Energy Conversion and Management 348 (2026) 120621

Contents lists available at ScienceDirect

Energy Conversion and Management

journal homepage: www.elsevier.com/locate/enconman

Research Paper

Techno-economic assessment of Power-to-Ammonia-to-Power for long-term energy storage

Valentina Veltroni [a,*], Mattia Calabrese [a], Carlo Carcasci [a], Marco Pagliai [b]

[a] University of Florence, Department of Industrial Engineering (DIEF), Via di Santa Marta, 3, 50139 Florence, Italy
[b] University of Florence, Department of Chemistry 'Ugo Schiff' (DICUS), Via della Lastruccia, 3-13, 50019 Sesto Fiorentino, Italy

ARTICLE INFO

Keywords:
Green Ammonia
Renewable Energy Storage
Multi Energy System
Power-to-Hydrogen-to-Power
Power-to-Ammonia-to-Power
Haber-Bosch Modeling

ABSTRACT

Hydrogen produced via electrolysis represents a promising solution for renewable energy storage due to its high gravimetric energy density. However, its low volumetric density requires storage under extreme conditions, raising costs and safety concerns. An alternative approach involves converting hydrogen into other chemicals. Among them, ammonia offers higher volumetric energy density and lower tanks cost than hydrogen, stability under ambient conditions, and an existing transport infrastructure.

This study evaluates the techno-economic feasibility of green ammonia as an energy storage medium compared to green hydrogen. Green ammonia is synthesized using renewable electricity to power an electrolyzer, an air separation unit, and a Haber-Bosch reactor. Stored ammonia is later reconverted into electricity via a combined cycle gas turbine. The system is modeled using MESS, an open-source software developed at the University of Florence. The ammonia synthesis plant model includes reaction kinetics and flexible operation. System sizing is performed by minimizing the Levelized Cost of Electricity (LCOE), assuming a 4 MW electricity demand at each hourly step over a year, fully supplied by photovoltaics coupled with ammonia or hydrogen storage.

A sensitivity analysis on the load profile reveals that ammonia is more cost-effective for long-duration storage, provided reactor operation is properly controlled. Under constant and winter–peaked demand, ammonia achieves LCOEs of 0.529 €/kWh and 0.666 €/kWh, outperforming hydrogen at 0.575 €/kWh and 1.209 €/kWh. With summer-peaked demand, characterized by short–term storage needs, hydrogen reaches 0.343 €/kWh, whereas ammonia 0.483 €/kWh. Battery-integrated variants are also assessed, reducing LCOE in all scenarios except for the hydrogen-based system under summer-peaked demand.

1. Introduction

Tackling climate change is at the heart of the European Union's energy policy. Under the European Green Deal, the EU has committed to achieving climate neutrality by 2050, with an intermediate target of at least a 55 % reduction in net Greenhouse Gas (GHG) emissions by 2030 relative to 1990 levels, as outlined in the "Fit for 55" package [1].

Renewable energy sources, particularly wind and solar, are pivotal to this transition. However, their intermittency poses a critical challenge: the success of a fully decarbonized energy system depends on continuous matching between variable, non-dispatchable renewable generation with real-time demand. Currently, this balance is compromised by frequent curtailment of surplus electricity during peak production, alongside the inability to meet demand during periods of low output. This underscores the urgent need for scalable, long-duration, and transportable energy storage solutions. Among the available options, chemical storage in the form of hydrogen is widely recognized as a leading candidate. Hydrogen enables long-term, large-scale storage and can be transported using a dedicated infrastructure. However, its low volumetric energy density necessitates storage at high pressure or cryogenic temperatures, leading to substantial technical and economic challenges. To address these limitations, alternative hydrogen carriers are being explored. Solid-state hydrogen storage options include methods such as metal–organic frameworks, carbon-based nanomaterials, metal hydrides, and complex hydrides. These approaches, while promising, often face challenges with reversibility and costs [2].

A more viable pathway involves converting hydrogen into other

* Corresponding author.
E-mail addresses: valentina.veltroni@unifi.it (V. Veltroni), mattia.calabrese@unifi.it (M. Calabrese), carlo.carcasci@unifi.it (C. Carcasci), marco.pagliai@unifi.it (M. Pagliai).

https://doi.org/10.1016/j.enconman.2025.120621
Received 21 July 2025; Received in revised form 23 September 2025; Accepted 1 October 2025
Available online 14 October 2025

Nomenclature

Acronyms

AICR	Adiabatic Indirect Cooled Reactor
ASU	Air Separation Unit
ASR	Ammonia Synthesis Reactor
BOP	Balance Of Plant
CAPEX	Capital Expenditure
CCGT	Combined Cycle Gas Turbine
COP	Coefficient Of Performance
GHG	Greenhouse Gas
HB	Haber-Bosch
LCOA	Levelized Cost Of Ammonia
LCOE	Levelized Cost Of Electricity
LOC	Level Of Charge
MESS	Multi Energy System Simulator
MILP	Mixed-Integer Linear Programming
NTU	Number of Transfer Unit
ODE	Ordinary Differential Equations
OPEX	Operational Expenditure
PEMEL	Proton Exchange Membrane Electrolyzer
PSA	Pressure Swing Adsorption
PV	Photovoltaic
PVGIS	Photovoltaic Geographical Information System
P2A	Power-to-Ammonia
P2A2P	Power-to-Ammonia-to-Power
RHE	Recuperative Heat Exchanger
SEC	Specific Energy Consumption
SOC	State Of Charge
SOFC	Solide Oxide Fuel Cell
TMY	Typical Meteorological Year
VLE	Vapour Liquid Equilibrium
WACC	Weighted Average Cost of Capital

Symbols	**Meanings (Units)**
a	Activity (−)
C	Cost (€)
E	Energy (kWh)
i	Discount rate (−)
LHV	Lower Heating Value (kJ/kg)
LOC	Level of charge (t)
m	Mass (kg)
$\dot{m}$	Mass flow rate (kg/s)
n	Duration (years)
k	Reaction rate constant ($kmol_{NH3}/(h{\cdot}m^3)$)
K_{eq}	Reaction equilibrium constant (−)
p	Pressure (atm or bar)
P	Power (kW)
r_{NH_3}	Reaction rate ($kmol_{NH3}/(h{\cdot}m^3)$)
SOC	State of charge (kJ)
t	Timestep (h)
T	Temperature (K)
V	Volume (m^3)
X_{N_2}	Nitrogen conversion (−)
y	Molar fraction (−)
α	Kinetic constant (−)
Δ	Difference (−)
ε	Effectiveness (−)
η	Efficiency (−)
ς	Specific energy production (kWh/kW_p)
σ	Battery self-discharge rate (−)

Subscripts

BT	Battery
ch	Charge
dis	Discharge
eq	Equilibrium
fuel	Fuel
H_2	Hydrogen
in	Inlet
N_2	Nitrogen
NH_3	Ammonia
out	Outlet
p	Pressure
r	Rated
rep	Replacement

chemical compounds, including ammonia, synthetic hydrocarbons like methanol and methane, or liquid organic hydrogen carriers such as methylcyclohexane and toluene [2]. These compounds not only provide efficient hydrogen storage but, in some cases, can also be used directly as fuels. Among these options, ammonia (NH_3) stands out due to its favorable properties and mature industrial infrastructure. It liquefies at –33 °C at atmospheric pressure (or under moderate pressure at ambient temperature), has a high volumetric hydrogen content (121 kg_{H2}/m^3), and can leverage existing global infrastructure, including pipelines, ships, railcars, and storage tanks [3].

Ammonia production currently exceeds 176 million tonnes per year, with over 70 % used for fertilizers. The dominant production process combines steam methane reforming to generate hydrogen with Haber-Bosch (HB) synthesis, accounting for nearly 2 % of global CO_2 emissions and consuming 3–5 % of the world natural gas, and up to 2 % of its total energy demand [4]. As a low-carbon alternative, green ammonia is produced from water and air using renewable electricity: hydrogen is generated via electrolysis, nitrogen via air separation, and both are fed into an HB reactor without fossil inputs. This process is commonly referred to as Power-to-Ammonia (P2A). While emerging alternative production methods, such as electrochemical ammonia synthesis, may offer higher efficiency beyond 2030 [5], optimizing the conventional Haber-Bosch process remains the most practical short-term option. However, unlike fossil-based ammonia plants designed for continuous, steady-state operation, green ammonia systems must handle fluctuating renewable energy inputs. This necessitates HB reactors capable of stable performance at partial loads, typically down to 20–30 % of nominal capacity [6], and limits the feasibility of frequent shutdowns due to the reactor long cold-start time (1–2 days), making load flexibility and operational continuity critical design requirements for P2A systems [7].

Beyond its role as a fertilizer, green ammonia is gaining attention as a versatile energy carrier [8]. It can be used directly as a fuel (in internal combustion engines, gas turbines, or marine engines), as a feedstock for fuel cells or cracked back into hydrogen for various downstream applications [3,4,8,9]. When ammonia is synthesized from renewable electricity and later reconverted into power, the process is referred to as Power-to-Ammonia-to-Power (P2A2P).

Most techno-economic studies focus on the P2A systems, aiming to minimize the Levelized Cost of Ammonia (LCOA). Some assume operating the reactor at a constant nominal load and propose strategies to maintain this condition during periods of low renewable availability [10–12], while others do not define the reactor operational constraints and limitations [13–15]. More comprehensive analyses move toward more realistic representations by incorporating partial-load operation and flexible scheduling of the HB reactor [6,16–24]. To support the HB reactor and the air separation unit during renewable shortfalls, additional power sources such as batteries are considered, while hydrogen is supplied to the HB reactor by a hydrogen buffer. Many of these studies

highlight that HB reactor flexible operation reduces curtailment and hydrogen storage requirements, critical factors for the economic viability of off-grid P2A systems [6,16–18,20–22,24], and also explore the integration of multiple renewable energy resources to mitigate intermittency [16,19,20,24]. Smith et al. [16], Tully et al. [18] and Campion et al. [19] applied linear programming, while Nayak–Luke [24] performed an optimization over multiple combinations of plant size and renewable energy mix, all assuming constant HB process consumption. Armijo et al. [20] introduced an HB power consumption model with fixed and variable components based on hydrogen input flow, solved through a matrix-based optimization. Wang et al. [21], Zhou et al. [6], Wu et al. [22] and Allman et al. [23] applied a Mixed-Integer Linear Programming (MILP) model for capacity designing and/or scheduling, still assuming constant–efficiency HB process. Among P2A studies, Smith and Murciano [17] provide the most advanced representation, introducing a complete HB reactor model including partial-load operation and implementing a "surplus-deficit" scheduling algorithm for the reactor operation, reducing hydrogen storage needs.

Recently, interest in ammonia as an energy vector has driven significant research also in integrated Power–to–Ammonia–to–Power systems, addressing various aspects from thermodynamics [25–27] to techno-economic analyses [28–35]. Some studies focus solely on the P2A2P system [25,29,33,34], while others compare ammonia with alternative storage options [26–28,30–32,35]. Most of these works, however, generally do not explicitly model the operational flexibility of the ammonia synthesis reactor. Wen et al. [28] compared multiple P2A2P and biomass-to-ammonia-to-power scenarios, Muller et al. [26] and Wen et al. [30] examined ammonia versus hydrogen as energy carriers, Tsiklios et al. [27] extended this comparison to include methanol and methane, while Lan et al. [35] explored a hydrogen–ammonia combined operation strategy. None of these, however, consider a flexible ammonia synthesis process. Only a few works on P2A2P incorporate reactor constraints and load flexibility. Cesaro et al. [34] analyzed a P2A2P system including a battery and a combined cycle gas turbine (CCGT) under different ammonia/hydrogen blend scenarios, introducing a minimum load constraint for the HB reactor, but without modeling partial-load operation. Palys et al. [31,32] performed annual, hourly-resolved simulations for islanded microgrids, optimizing system sizing and energy management while including a low-pressure HB reactor with basic load control strategies, and also benchmarked ammonia storage against compressed green hydrogen. Rouwenhorst et al. [33] developed a P2A2P plant featuring a ruthenium–based catalyst reactor for intermittent operation in Aspen Plus, a metal–halide separation unit, and a solid oxide fuel cell for reconversion. Moreover, they combined the use of a battery for short-term energy storage and ammonia for long-term storage. Both Palys et al. [31,32] and Rouwenhorst et al. [33] considered the reactor model, but with technologies not yet commercially available.

Focusing on HB reactors operating at commercially relevant conditions (utilizing condensation to separate ammonia while working at high pressure), some studies explore detailed control to manage reactor load variability, but do not address the full P2A2P system or its economic feasibility. Gullberg [36], Fedrigo [37] and Patel et al. [38] performed dynamic simulations of flexible-load green ammonia plants using control strategies on synthesis temperature and pressure. Fahr et al. [39] optimized a reactor for high operational flexibility, analyzing thermodynamic properties and their impact on partial-load operation, while a subsequent work [40] included a reactor cost model and applied bi-objective optimization to balance flexibility and investment costs. Cheema et al. [41,42] evaluated different reactor types, assessing design and performance under off-design conditions by varying operating pressure, inert gas content, NH_3 concentration, reactant flow rate, reactant temperature, and H_2/N_2 ratio.

Overall, these studies highlight the lack of comprehensive techno-economic analyses of islanded systems comparing Power-to-Hydrogen-to-Power and Power-to-Ammonia-to-Power, including a detailed model of the ammonia synthesis loop that considers both its flexibility and operational constraints.

1.1. Aims of the study and novelty

Most existing analyses on green ammonia focus on production (P2A), primarily aiming to minimize the Levelized Cost of Ammonia under intermittent renewable energy inputs. In contrast, techno–economic evaluations of integrated Power-to-Ammonia-to-Power systems remain limited, and the modeling of the ammonia synthesis process, when addressed, is often simplified, with little attention paid to reactor behavior under flexible operation and off-design conditions. In the few cases where flexibility is modeled, it typically involves advanced technologies that are not yet commercially available.

Unlike previous studies, this work evaluates a P2A2P system including a detailed model of the ammonia synthesis loop that reflects current reactor technology, accounts for partial-load operation, and explicitly incorporates flexibility and shutdown constraints.

The study encompasses the entire P2A2P chain from renewable electricity generation through electrolysis, nitrogen separation, and ammonia synthesis, to storage and reconversion to electricity. At the core of this framework there is a physically based, parametrized model of the Haber-Bosch reactor, embedded within a custom-developed energy system simulation tool. This approach enables a detailed representation of reactor dynamics, including part–load operation, ramping constraints, and load–dependent energy consumption. The system is simulated at hourly resolution over a full year to capture both seasonal and intraday variability in renewable energy availability.

The primary objective of this work is to compare hydrogen and ammonia as renewable energy storage media from a techno-economic perspective. All system components are sized through an optimization process that minimizes the Levelized Cost of Electricity (LCOE), with a focus on off-grid configurations where storage and flexibility are critical. Through sensitivity analyses on the demand profile, the study identifies the conditions under which ammonia becomes a more cost-effective storage option than hydrogen, also considering battery integration for short-term storage. These findings aim to clarify the role of ammonia in long-duration energy storage systems powered by variable renewables.

2. Materials and methods

The comprehensive analysis presented in this study is conducted using the open-source software Multi Energy System Simulator (MESS) [43], co-developed by the authors and collaborators. MESS is written in Python and features a modular architecture that enables the simulation of a wide range of energy systems, as well as detailed modeling of system components under both design and off-design operating conditions. The simulation framework follows a rule-based operational logic, governed by a predefined hierarchy of intervention priorities among system components. For further details on MESS energy management strategies, the reader is referred to refs. [44–47].

For this study, a dedicated modeling framework for ammonia-based renewable energy storage has been developed and integrated into MESS. Existing hydrogen technology models were extended and adapted to include ammonia synthesis and reconversion processes, enabling a comprehensive assessment of Power-to-Ammonia-to-Power systems.

The analysis is conducted using energy and mass balances with an hourly time resolution.

The remainder of this section is organized as follows: Section 2.1. outlines the system configuration for both hydrogen-based and ammonia-based energy storage. Sections 2.2. to 2.10. describe the modeling approach adopted for the individual components, with emphasis on the ammonia synthesis reactor and its operational parameters (Section 2.8.). Section 2.11. details the energy allocation strategy implemented to coordinate system operation. Section 2.12. introduces the case studies used to compare ammonia and hydrogen as renewable

energy storage solutions and details the sizing methodology aimed at minimizing the Levelized Cost of Electricity.

2.1. Systems configuration

Given the focus on evaluating ammonia and hydrogen as renewable energy storage solutions, the analysis is conducted under an islanded system configuration. In this setup, the electrical load must be entirely met by a Photovoltaic (PV) plant and the associated storage system, without any grid connection.

The hydrogen-based configuration includes a PV system, a Proton Exchange Membrane Electrolyzer (PEMEL), a hydrogen compressor, a hydrogen storage tank, and a Combined Cycle Gas Turbine (CCGT) which reconverts stored hydrogen into electricity.

The ammonia-based system builds upon this architecture by incorporating an Ammonia Synthesis Reactor (ASR), which comprises the entire ammonia synthesis loop including compressors, heat exchangers, separator, and the catalytic beds of the Haber-Bosch process, an Air Separation Unit (ASU) – modeled as a Pressure Swing Adsorption (PSA) system – to supply nitrogen, and an ammonia storage tank. In this case, the CCGT operates directly using ammonia as fuel.

Moreover, in a subsequent case study, both systems are further extended by the addition of a battery for short-term balancing.

In both configurations, the operational logic prioritizes covering the electrical demand using direct PV generation. When surplus renewable electricity is available, it is diverted to produce hydrogen or ammonia for storage. When a battery is integrated, surplus electricity first charges the battery, and any remaining excess is sent to produce hydrogen or ammonia. During discharge, the battery is also used with priority over the chemical storage system. The two configurations are illustrated in Fig. 1, while Table 1 summarizes the operating conditions and technical parameters selected for each component. In Fig. 1, the battery is depicted with a dashed outline to indicate that it is an optional component, included only in the subsequent battery-integrated case study.

In the ammonia-based system, both the ASR and the PSA must operate continuously, even in the absence of renewable electricity. To ensure this, the CCGT also supplies auxiliary power to these units, in

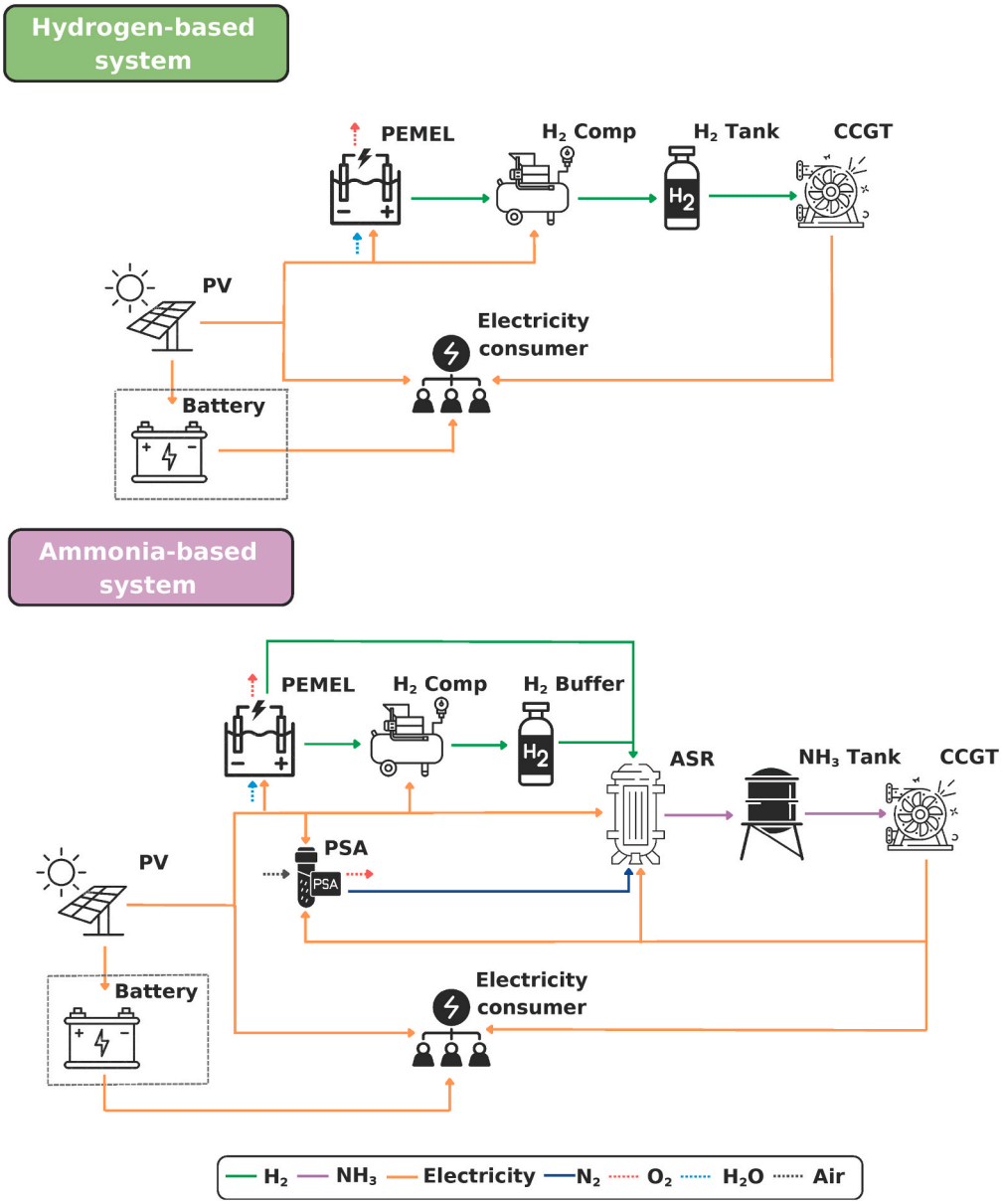

Fig. 1. Schematic comparison of the two integrated energy storage systems: the hydrogen-based system (top) and the ammonia-based system (bottom).

Table 1
Components nominal operating conditions and technical parameters.

Component	Parameter	Units	Value	Reference
Tracking PV	Tracking system	–	Single horizontal axis aligned N-S	Own assumption
	Losses	%	10	[48]
	Ref. year	–	TMY	[49]
Battery	Charging efficiency	%	92	[50]
	Discharging efficiency	%	92	[50]
	Minimum SOC	% of nominal capacity	20	[50]
	Self-discharge rate	%/month	5	[50]
PEMEL	Single stack power	kW	1000	[33]
	Operating pressure	bar	30	[45]
	Operating temperature	°C	70	[45]
	Nominal efficiency	kWh/kg_{H2}	55.54	[45]
	Minimum stack load	%	5	[33]
H_2 Compressor	Inlet pressure	bar	30	Own assumption
	Outlet pressure	bar	210	Own assumption
	Number of stages	–	2	Own assumption
	Polytropic efficiency	%	70	[51]
H_2 Tank	Operating pressure	bar	200	[17]
	Minimum LOC	% of maximum capacity	9 (H_2 system)	Own assumption
			15 (NH_3 system)	Own assumption
PSA	Number of compression stages	–	2	Own assumption
	Compressor polytropic efficiency	%	85	[10]
	Operating pressure	bar	7	[52]
	Operating temperature	°C	25	[52]
	Minimum unit load	%	30	[53]
	Air factor	Nm^3_{air}/Nm^3_{N2}	5.2	[52]
	Unit maximum size	Nm^3_{N2}/h	400	[52]
ASR	Operating pressure	bar	150	[54]
	Beds inlet temperature	°C	390, 420, 410	[54]
	Maximum ramp-rate	%	± 30	[22]
	Minimum load	%	30	[55]
	Compressors polytropic efficiency	%	85	[10]
	Condenser temperature	°C	−10	Own assumption
	Refrigeration cycle COP	–	3	Own assumption
NH_3 Tank	Operating pressure	bar	18	[56]
	Minimum LOC	% of maximum capacity	0	Own assumption
CCGT	Efficiency	%	52	[57]

addition to meeting the electricity demand. Moreover, a dedicated hydrogen buffer tank is employed to decouple the intermittent operation of the PEMEL from the continuous hydrogen demand of the ASR. Supplying the hydrogen required by the ASR directly from the electrolyzer powered by the CCGT when no renewable energy is available would be impractical due to the PEMEL very high energy consumption, so part of the hydrogen produced during periods of renewable energy availability is stored for later use. This setup ensures process stability, as frequent shutdowns and restarts are not technically viable for the Haber-Bosch process.

2.2. Photovoltaic system

The energy production of the photovoltaic system is simulated using the PVGIS platform [49] to retrieve hourly solar irradiance data and modeled PV power output, providing as input a predefined set of parameters including geographic location, system configuration, and assumed system losses. In particular, the PVGIS-SARAH 3 dataset is employed to provide these data based on a Typical Meteorological Year (TMY). The selected site corresponds to the rural area surrounding the city of Florence, with a latitude of 43.76° N and a longitude of 11.25° E. The system adopts a single-axis tracking configuration, with the axis oriented along the north–south direction. Total system losses are

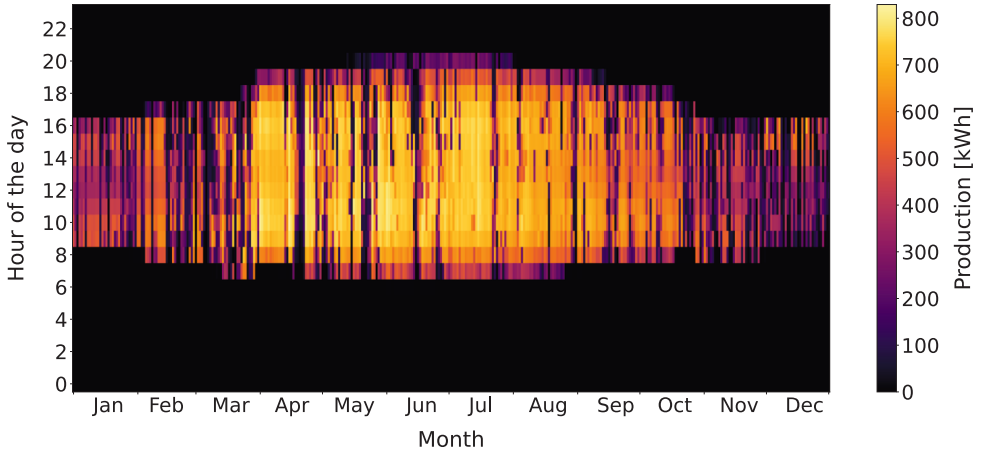

Fig. 2. Hourly PV production throughout the year for a 1 MW installed capacity.

assumed to be 10 % [48].

Under these conditions, the system yields a capacity factor of approximately 20 %, resulting in an annual energy production of around 1750 kWh/kW_p, with the hourly trend reported in Fig. 2.

This modeling approach provides a time-dependent specific energy yield $\zeta_{PV}(t)$, which is used to compute the total PV power output $P_{PV}(t)$ by multiplying it by the nominal power of the plant $P_{PV,r}$, as expressed in Equation (1):

$$P_{PV}(t) = \zeta_{PV}(t) \bullet P_{PV,r} \quad (1)$$

2.3. Battery

The battery selected for this study employs lithium-ion technology, which offers higher efficiency, longer lifespan, and better energy density compared to lead-acid alternatives [58]. The State of Charge (SOC), representing the stored energy, is updated dynamically at each timestep following Equation (2):

$$SOC(t+1) = SOC(t) \bullet (1-\sigma) + P_{BT,ch}(t) \bullet \Delta t \bullet \eta_{BT,ch} - \frac{P_{BT,dis}(t) \bullet \Delta t}{\eta_{BT,dis}} \quad (2)$$

Where $\eta_{BT,ch}$ and $\eta_{BT,dis}$ are respectively the battery charging and discharging efficiencies and σ is the hourly self-discharge rate. To prevent deep discharge and ensure safe operation, the battery SOC is maintained between 20 % and 100 % of its nominal capacity.

2.4. Electrolyzer

The selected electrolyzer type is PEMEL due to its fast start-up capability and low minimum load, which makes it particularly well-suited for dynamic operation [7,33,53]. Moreover, PEMEL technology ensures a high hydrogen purity level (99.999 %) [53], allowing its direct use in the ASR. The modeling approach adopted for the electrolyzer is detailed by Lubello et al. [45], with operating conditions set at 30 bar and 70 °C.

Each stack is assumed to have a maximum power of 1 MW, which represents the typical upper limit for commercial PEMEL units [33], and a minimum operational load of 5 % of the nominal power [33]. The load is defined as the ratio between the electrical power supplied to the electrolyzer and its nominal rated power. Electrical power is distributed in parallel among the stacks: if the available power is sufficient, all modules operate uniformly above the minimum threshold; if not, the system dynamically reduces the number of active stacks to ensure that those remaining can operate above the minimum load.

The nominal efficiency of each stack, defined as the ratio between the hydrogen lower heating value and the electrical energy supplied, is 60 %, corresponding to a specific energy consumption of 55.54 kWh/kg_{H2} [45]. The variation of efficiency of the PEMEL stack with respect to the load is shown in Fig. 3.

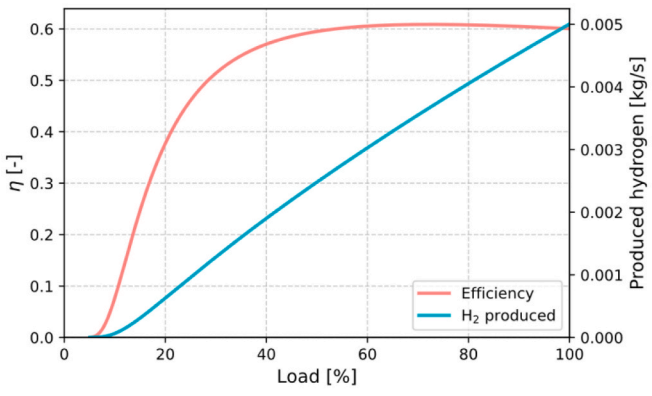

Fig. 3. Electrolyzer stack efficiency (red line) and hydrogen production mass flow rate (sky-blue line) under varying load conditions.

2.5. Hydrogen compressor

In both the ammonia-based and hydrogen-based systems, hydrogen is stored in a tank at a pressure of 200 bar.

To compress hydrogen from the electrolyzer outlet pressure of 30 bar to the storage pressure, a piston–type compression system is employed. The compressor outlet pressure is set at 5 % more than the tank storage pressure to prevent backflow. The compression process is modeled assuming a polytropic efficiency of 70 % [51]. Depending on the hydrogen tank state of charge, i.e. its internal pressure, either one or two compression stages are activated during operation. The electrical energy consumption of the compressor is estimated by considering the isentropic efficiency (variable with load) and applying the thermodynamic relationships provided in Section S1 of the Supplementary Material. The resulting nominal specific consumption is 1.5 kWh/kg_{H2}.

2.6. Hydrogen tank

In both configurations, hydrogen is stored at 200 bar using a Type I pressure vessel [17]. The Level Of Charge (LOC) of the hydrogen tank, defined as the mass of hydrogen currently stored inside the tank, is dynamically updated at each simulation time step t. The evolution of the LOC accounts for the net balance between the mass of hydrogen directed to the tank $m_{H_2,in}$ and the mass of hydrogen withdrawn for consumption $m_{H_2,out}$ and is described by Equation (3).

$$LOC(t+1) = LOC(t) + m_{H_2,in}(t) - m_{H_2,out}(t) \quad (3)$$

The LOC oscillates between the minimum level of charge and the tank maximum capacity throughout the year.

Since hydrogen is stored in gaseous form, the tank pressure varies with the LOC. A minimum level of charge is therefore required to maintain a pressure equal to or above ambient pressure. In the ammonia-based system, the minimum buffer level is set to 15 % of the tank maximum capacity, ensuring that the inlet pressure to the ASR remains at least at the design value of 30 bar, which corresponds to the nominal outlet pressure of the electrolyzer. In the hydrogen–based system, the minimum LOC is set to 9 % of the total capacity, ensuring a minimum pressure of approximately 18 bar. This matches the pressure level maintained in the ammonia tank of the ammonia-based system, as both configurations supply the downstream CCGT.

2.7. Air separation unit

Cryogenic distillation, accounting for 65–70 % of global nitrogen production, can deliver ultra-high purity N_2 (up to 50,000 Nm^3_{N2}/h, <1 ppm O_2) with relatively low energy use (~0.11 MWh/t_{N2}) thanks to internal heat integration [53,59]. However, this integration limits flexibility: units require hours to start and cannot operate below ~ 60 % load, making them unsuitable for variable operation [7,53].

To enable greater operational flexibility and dynamic response, pressure swing adsorption technology has been selected for nitrogen production in this study. PSA is a cyclic separation process in which nitrogen is extracted from compressed air by selectively adsorbing oxygen onto a solid adsorbent, typically a carbon molecular sieve, at near ambient temperature. The process operates over pressure cycles, with adsorption typically occurring at 6–8 bar, followed by desorption at approximately 1 bar [53,60]. PSA systems are modular and compact, offering rapid startup and the ability to operate down to 30 % of nominal capacity [53]. A hybrid cryogenic ASU–PSA system was also possible but was not considered in this analysis, since the nitrogen unit has only a minor impact on cost and energy compared to the other system components.

The PSA configuration modeled in this study consists of a central air

compression system and multiple adsorption modules, each made up of two alternating beds. Energy consumption is modeled by simulating the air compression process in design and off-design conditions using the equations detailed in Section S1 of the Supplementary Material. A key modeling parameter is the air factor, defined as the volumetric amount of compressed air required to extract a given volume of nitrogen. Based on the specifications from the Pneumatech PPNG 150–800 HE series [52], designed for flexible operation with an adaptive internal control algorithm, the air factor is assumed to remain constant at 5.2 Nm^3_{air} / Nm^3_{N2}, even under partial load conditions. To meet the requirement of 99.999 %, which suppliers indicate as the minimum level needed to avoid catalyst poisoning [53] and also avoid purge losses in the ASR, the size of each adsorbent column unit is limited to 400 Nm^3_{N2}/h [52], which is the maximum capacity for the considered model corresponding to the required purity. Higher purity significantly reduces production capacity while installation and operating costs remain approximately the same.

2.8. Ammonia synthesis reactor

The Haber-Bosch process remains the only commercially available method for large-scale ammonia production [61]. Standard HB reactors operate with catalytic beds at high pressures and employ iron–based catalysts, while ammonia separation is achieved through condensation [5]. Although ruthenium-based catalysts exhibit superior activity, their high cost remains a significant barrier to large–scale deployment [7]. Similarly, adsorption–based separation technologies, which could enable lower pressure operation, are still under development and not yet commercially mature [7].

Ammonia synthesis is an exothermic reaction that is thermodynamically favored at low temperatures. However, slow kinetics under such conditions require elevated pressures (150–300 bar) and temperatures (350–525 °C) for industrial implementation, typically within reactors featuring multiple catalytic beds [62]. Hydrogen and nitrogen are introduced at a stoichiometric molar ratio of 3:1 [4]. Given the relatively low single-pass conversion efficiency (15–30 %), unreacted gases are continuously separated and recycled to increase the overall yield [4].

The ammonia synthesis reaction is as follows [4]:

$$N_2 + 3H_2 \rightleftharpoons 2NH_3; \Delta H_{298K} = -92 \frac{kJ}{kmol} \quad (4)$$

Ammonia is condensed by cooling the effluent from the last catalytic bed to −20 to 30 °C (depending on the working pressure), while the remaining hydrogen and nitrogen are mixed with fresh feedstock and recirculated [7]. A small fraction of ammonia (typically 2–5 mol%) is reintroduced into the first catalytic bed through the recycle stream [7]. Given the exothermic nature of ammonia synthesis, the heat released during the reaction is recovered to preheat the incoming reactants.

In the modeled system, hydrogen and nitrogen are compressed separately, as they originate from different upstream units which operate at distinct pressure levels. Moreover, hydrogen may be sourced from a partially pressurized storage buffer rather than directly from the electrolyzer, requiring the flexibility to bypass certain stages or shut down the entire hydrogen compression line. After compression, the reactants are mixed with the recycled unreacted gases and preheated. A Recuperative Heat Exchanger (RHE) recovers thermal energy from the hot effluent exiting the series of catalytic beds to bring the mixture to its target inlet temperature to the first catalytic bed. The modeled system features a three-bed Adiabatic Indirect Cooled Reactor (AICR), currently the most widely adopted configuration due to its favorable trade-off between conversion efficiency and cost [41]. The effluent from the series of catalytic beds is then cooled in three stages: initially via the RHE, then through a water-cooled heat exchanger, and finally by a refrigeration cycle. The latter is essential to reach sufficiently low temperatures for efficient ammonia condensation while ensuring minimal residual ammonia content in the recycle stream and maintaining moderate operating pressures. The schematic representation of the plant configuration is shown in Fig. 4.

Operating the ammonia synthesis reactor under variable loads introduces significant challenges, primarily related to process instability (e.g. limit cycles or shutdowns) and catalyst overheating due to prolonged residence times at reduced flow rates [38].

This study focuses on steady-state operation, assuming that if key operational limits are respected, the system remains within a stable and safe regime during transient phases. Under this assumption, the following constraints are imposed:

- Constant pressure and temperature at design-point values at the inlet of the catalytic beds, regardless of load, to prevent plant instability and ensure reliability [37,38].
- Constant condensation temperature to avoid fluctuations in ammonia concentration of the recirculated gases that could overheat the catalyst [36–38,63].
- Continuous ammonia synthesis reactor operation, avoiding start-ups due to their time and energy intensity, and a maximum ramp rate of ± 30 % per hour to avoid thermal stresses of the catalyst [22].
- A minimum load of 30 % of the nominal capacity, dictated by standard equipment turndown limits [55].

The inlet temperature of the first catalytic bed is controlled using a quench valve upstream of the beds, which regulates the flow by bypassing the recuperative heat exchanger [38,63]. If heat recovery is insufficient, an auxiliary preheater maintains the target inlet temperature [36]. The temperature of the second and third catalytic bed is assumed to be controlled by varying cooling water flow rates.

Pressure is controlled by modulating the recycle compressor power, preventing imbalances when the fresh reactant feed is reduced [37].

Condensation temperature is kept constant via partial-load operation of the refrigeration cycle [36,37].

To ensure uninterrupted ASR operation during periods of low hydrogen production from PEMEL, a hydrogen buffer is included. The buffer stores hydrogen produced during renewable surplus and supplies it to the ASR to maintain minimum load or respect ramp-rate constraints. In parallel, a small amount of ammonia is burned in the CCGT to provide the electrical power needed by auxiliary components such as the PSA and synthesis loop.

The electricity consumption of the ammonia synthesis loop includes the fresh feed compressors, the recycle compressor, and the refrigeration cycle. To estimate these energy demands and ensure compliance with the operating temperature constraints, the entire loop is simulated using a detailed kinetic model of the reaction. Two main sections can be identified: one dedicated to reactant preparation (Section 2.8.1. and the other to the synthesis loop (Section 2.8.2.).

The main assumptions adopted for the simulation are as follows:

- No pressure drops are considered within the single components. A pressure reduction of 6 % relative to the operating pressure is assumed downstream of the separator to account for the total pressure losses across the loop [36,64]. Under partial load conditions, this pressure drop scales with the square of the flow rate.
- Impurities such as argon are neglected. For green ammonia production, both hydrogen and nitrogen are assumed to be of very high purity (99.999 %). Given the high purity of the synthesis gas, purging is deemed unnecessary [37,65]. A deoxo unit for removing trace amounts of O_2 from nitrogen and hydrogen should be considered [7], but is neglected since the feed gases are already highly pure and its impact on costs would be negligible.
- Compressors discharge pressures are maintained constant. The fresh feed compressors modulate the flow rates based on reactant availability, while the recycle compressor adjusts the flow according to the partial load conversion rate and the resulting variation in the recirculation-to-fresh feed ratio, ensuring stable loop pressure.

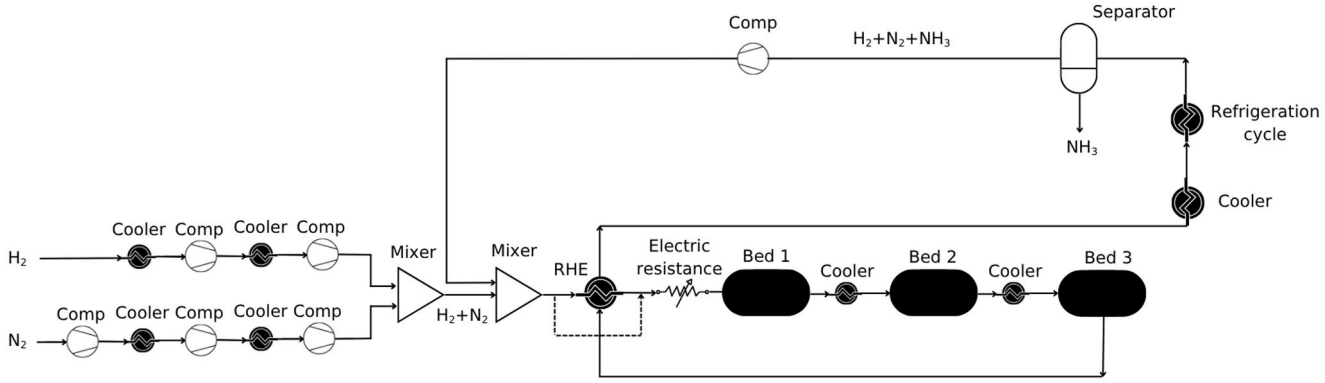

Fig. 4. Layout of the ammonia synthesis reactor, including the reactants preparation section with compressors and heating, three catalytic beds with indirect cooling, ammonia condensation and separation, and a recirculation loop featuring a compressor.

- The inlet temperatures of the catalytic beds, the condensing temperature, and the temperatures of the intercoolers are all maintained at constant values.

2.8.1. Compression and heating of reactants

Compressors power consumption in design and off-design conditions is modeled using the approach reported in Section S1 of the Supplementary Material.

All mixing processes throughout the plant are assumed to be adiabatic and evaluated through enthalpy balances.

The thermal energy required to raise the temperature of the reactants is recovered from the hot gas stream exiting the third catalytic bed. The recuperative heat exchanger is designed to maximize heat recovery, with a pinch point temperature difference of approximately 20 °C. Under this assumption, the RHE may be oversized with respect to the heat demand under nominal conditions. However, this design choice is intentional, as it helps to prevent critical situations during dynamic transients or partial load operation.

The design effectiveness and surface area of the RHE, modeled as a counter-current heat exchanger with concentric tubes, are determined using the ε-NTU method. In off-design conditions, the RHE effectiveness is evaluated using the design heat transfer area, the updated value of the rates of the thermal capacities of the two fluids, and the recalculated off-design value of the overall heat transfer coefficient. The detailed equations used for both design and off-design conditions are given in Section S2 of the Supplementary Material.

If the recovered heat raises the gas temperature above the desired inlet temperature of the first catalytic bed, an iterative bypass control is applied to divert a fraction of the stream around the RHE. Conversely, if heat recovery is insufficient, an electric preheater is activated. However, rather than relying on electrical heating, it is generally preferable to modify the system configuration to recover heat from intermediate catalytic beds.

2.8.2. Catalytic beds and recirculation loop

The synthesis loop is simulated through an iterative procedure that includes both reaction kinetics within the catalytic beds and ammonia condensation.

The catalytic beds model is developed and validated using the methodology presented by Jorqueira et al. [54]. Given the high-pressure and high–temperature operating conditions, the Peng–Robinson equation of state is used to describe the thermodynamic behavior of the system. The catalytic beds are modeled as plug-flow, assuming no axial mixing and complete radial mixing. Pressure is considered constant along the beds, as pressure drops are minimal and do not significantly affect reaction kinetics [41]. Pressure losses are accounted for downstream, as discussed earlier.

The reaction rate, defined as the moles of ammonia produced per m^3 of catalytic bed and per unit time, is described using the modified Temkin equation, presented in Equation (5) [66,67].

$$r_{NH_3} = k \bullet \left(K_{eq}^2 \bullet a_{N_2} \bullet \left[\frac{(a_{H_2})^3}{(a_{NH_3})^2} \right]^{\alpha} - \left[\frac{(a_{NH_3})^2}{(a_{H_2})^3} \right]^{1-\alpha} \right) \quad (5)$$

Where r_{NH_3} is the reaction rate in $kmol_{NH3}/(h \cdot m^3)$, k is the reaction rate constant in $kmol_{NH3}/(h \cdot m^3)$, a is the activity, K_{eq} is the equilibrium constant of the reaction, and α is a constant describing the reaction order taken with a value of 0.57 [54]. Although ammonia synthesis is a heterogeneous reaction, the expression for r_{NH_3} represents the pseudo-homogeneous reaction rate in a packed bed, treating the catalyst and gas as a single phase and expressing the rate per unit bed volume. To account for mass transfer and intra-pellet diffusion, an effectiveness factor is applied to yield the corrected reaction rate.

Mass and energy balances along the catalytic beds are formulated as a system of Ordinary Differential Equations (ODEs), reflecting the continuous variation of gas properties along the catalytic beds due to the ongoing chemical reactions. The detailed equations used for the catalytic beds modeling, including both kinetics and ODEs, are presented in Section S3 of the Supplementary Information, while the procedure adopted for the validation of the catalytic beds model is detailed in Appendix A.

The recirculation loop calculation, in addition to the catalytic beds models, is necessary to determine the amount of ammonia condensed and the residual ammonia in the recirculated gas stream with H_2 and N_2. The marked difference in boiling points between ammonia and the other components of the mixture (H_2, N_2) allows to assume that the condensed ammonia stream is substantially pure [68]. Since the system operates under steady-state conditions with no purge stream, the total amount of condensed ammonia equals the combined mass flow rate input of nitrogen and hydrogen. The composition of the recirculated mixture is determined based on Vapour-Liquid Equilibrium (VLE), with detailed calculations provided in Section S4 of the Supplementary Information, along with the iterative calculation scheme of the recirculation loop. The power consumption of the refrigeration cycle is evaluated using a COP under off-design conditions, as detailed in Section S5 of the Supplementary Material.

2.8.3. Specific energy consumption profile

The operating pressure adopted for the three catalytic beds is 150 bar, with inlet temperatures of 390 °C, 420 °C, and 410 °C respectively [54]. The condensing temperature is set at −10 °C to maintain the ammonia mole fraction in the recirculating gas stream at approximately 4 % [7]. Considering the typical ratio between the recycled and fresh feed gases, that is generally two to three times the amount of fresh reagents, this operating condition results in an ammonia mole fraction of

around 3 % at the first bed inlet [54].

Once these conditions are defined, the volumes of the three catalytic beds are determined to reproduce the nitrogen conversion profile described in [54], which involves achieving approximately the same nitrogen conversion across each catalytic bed. This methodology is applied to a reference ammonia synthesis reactor producing 1 kg/s of ammonia (Fig. 5); however, the same conversion profile can be maintained for different ammonia synthesis reactor sizes by proportionally scaling the catalyst bed volumes according to the ammonia production rate of the loop.

Since the catalytic beds of Haber-Bosch reactors conventionally operate within a pressure range of 150 to 300 bar with iron catalysts, alternative possibilities are also explored by varying the operating pressure, as detailed in Appendix B. Operation at lower pressures is possible with costly catalysts such as ruthenium that have not been considered in this study. The analysis concludes that maintaining the pressure at 150 bar offers the most favorable operating conditions in terms of both energy consumption and operational safety.

Fig. 6 illustrates the Specific Energy Consumption (SEC) profile resulting from the selected operating parameters across the operating range of the Haber-Bosch synthesis loop, also highlighting its dependency on the percentage of hydrogen drawn from the buffer and the buffer pressure. The SEC curve reflects the off-design performance of key components such as compressors, the refrigeration cycle, and the recuperative heat exchanger.

When no hydrogen is drawn from the buffer (i.e. H_2 from buffer = 0 %), the minimum SEC occurs at approximately 80 % of the nominal load. Overall, the specific energy consumption ranges between 0.35 and 0.42 kWh/kg_{NH3}, which is consistent with values reported in the literature [64,69].

At partial load, the increase in compressor consumption is primarily due to reduced isentropic efficiency in the fresh feed compressors. The refrigeration cycle shows a minimum specific consumption near 50 % load, mainly influenced by the COP behavior and the reduced fraction of recycled gas. In fact, operating at partial load increases the residence time of gases within the catalytic beds, thereby enhancing the reaction conversion efficiency. For the RHE, dynamic bypass adjustment effectively maintains the desired temperature across all loads without requiring additional electric heating support.

Regarding hydrogen supply, when the buffer pressure is lower than the pressure downstream of the first compression stage, hydrogen from the buffer follows the same compression path as the electrolyzer–generated hydrogen, resulting in unchanged overall consumption. Conversely, consumption decreases progressively as the share of buffer hydrogen increases when the input pressure lies between the outlet pressures of the first and second compression stages, allowing the hydrogen to bypass one compression stage, or when the buffer pressure equals or exceeds the final discharge pressure of the compression train, in which case no additional compression is required.

2.9. Ammonia tank

Ammonia can be stored as a liquid using three main technologies: pressurized storage at ambient temperature (16–18 bar), semi-refrigerated storage near 0 °C and 3–5 bar, and atmospheric storage at –33 °C. A fourth, still experimental option is solid-state storage using materials like metal halides [56].

From an energy integration perspective, pressurized storage presents a strategic advantage over refrigerated systems. Since ammonia exits the synthesis loop at high pressures, typically between 150 and 300 bar, it can be stored directly without requiring further compression or refrigeration. This eliminates the energy demand associated with maintaining low temperatures, which would otherwise be necessary for atmospheric or semi-refrigerated storage. Moreover, when the downstream system (e.g. a power generation unit) operates using pressurized ammonia, pressurized storage enables a direct supply without the need for additional re-pressurization stages. For this reason, pressurized storage has been selected in this study.

In the present model, the evolution of the level of charge in the ammonia storage system is treated analogously to the hydrogen tank model (Equation (3)), with the simplifying assumption that the tank can be fully discharged since ammonia is stored in the liquid phase.

2.10. Power generation unit

Ammonia can be directly employed as a fuel for power generation in fuel cells, internal combustion engines, and gas turbines [3,70]. Solid Oxide Fuel Cells (SOFCs) are the most advanced fuel cell technology but suffer from limited flexibility due to high operating temperatures [3]. Internal combustion engines and gas turbines face combustion challenges related to ammonia low flame speed, high ignition temperature, and NO_x emissions [70,71]. These issues can be mitigated through combustion design and exhaust treatment [71].

Among the various technologies considered, ammonia-fired gas turbines represent the most mature and commercially promising option for near-term deployment [72]. Stable operation has been demonstrated up to the 2 MW scale, and commercial development is advancing rapidly. Mitsubishi Power plans to launch a 40 MW turbine by 2025, and larger systems (100 + MW) are under development in Japan, the Netherlands, and the U.S., with companies like IHI and GE Vernova leading efforts in retrofitting existing turbines and mitigating NO_x emissions. [59,73].

Given the imminent commercial viability of this technology, an ammonia-fueled gas turbine integrated into a combined cycle power

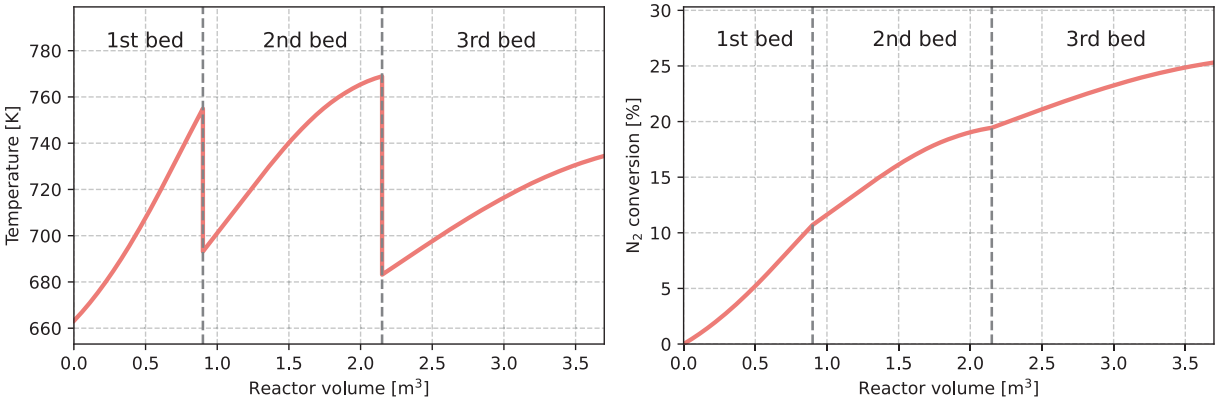

Fig. 5. Temperature (left) and nitrogen conversion (right) profiles along the three catalytic beds at the selected operational conditions for an ammonia synthesis reactor producing 1 kg_{NH3}/s.

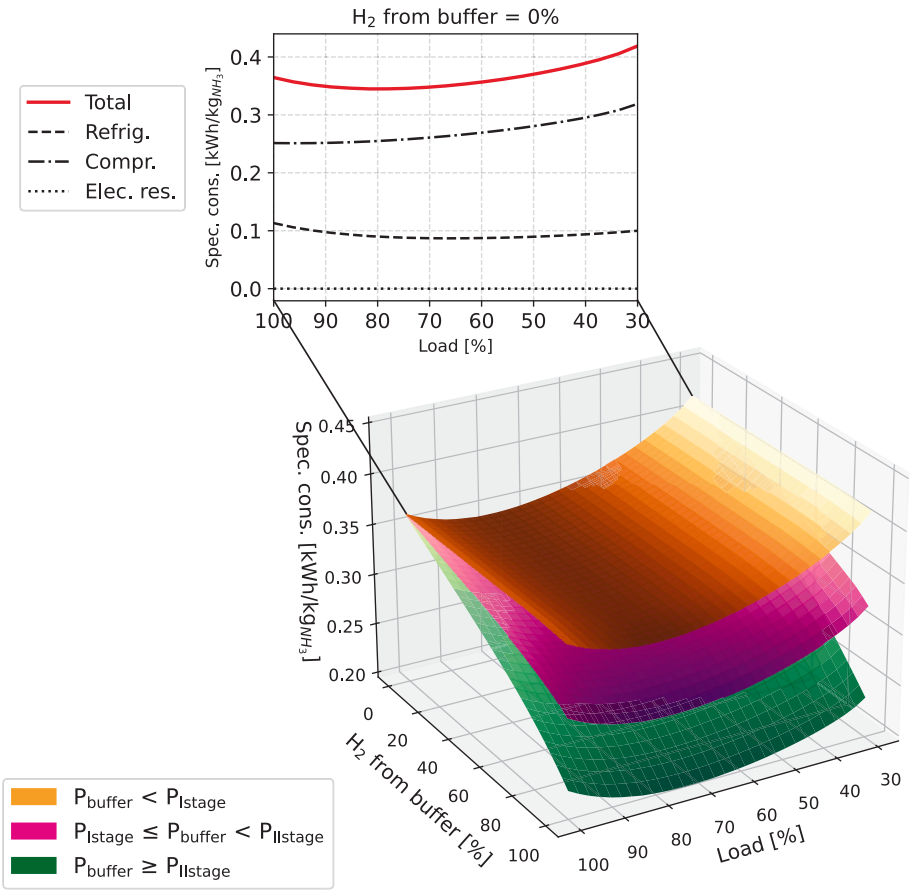

Fig. 6. The 3D plot shows specific electricity consumption of the ASR (z-axis) at varying load conditions (x-axis), hydrogen supply from the buffer (y-axis), and hydrogen from the buffer supply pressure (color scale). The buffer pressure (P_{buffer}) can be below the pressure at the end of the first compression stage (P_{Istage}), between the pressures at the end of the first and second stages, or above the pressure at the second stage ($P_{IIstage}$) of the hydrogen compression line inside the ASR. The inset 2D plot at 0 % hydrogen from buffer breaks down the consumption contributions: Refrig. = refrigeration cycle, Compr. = compressors, Elec. res. = electric resistance.

system has been selected for electricity generation for the ammonia-based case. For the hydrogen-based case, the CCGT is fueled by hydrogen.

The CCGT is modeled assuming an efficiency of 52 % [57], which allows for the determination of fuel (hydrogen or ammonia) consumption as a function of the electrical energy demand, as expressed in Equation (6).

$$\dot{m}_{\text{fuel}} = \frac{P}{\eta_{\text{CCGT}} \bullet LHV_{\text{fuel}}} \tag{6}$$

$\dot{m}_{\text{fuel}}$ is the fuel flow rate required to meet the load, P is the hourly power required, η_{CCGT} is the assumed combined cycle efficiency of 52 % and LHV_{fuel} is the lower calorific value of the fuel, equal to 18.6 MJ/kg for ammonia and 120 MJ/kg for hydrogen.

2.11. Energy allocation strategy

The system operates under a rule-based control logic that coordinates mass and energy flows on an hourly basis. Its primary objective is to satisfy the electrical demand while ensuring the continuous operation of critical components, namely the ASR and PSA.

The electrical load is primarily met using the available renewable energy. In the absence of sufficient PV generation, the CCGT is activated to compensate for the shortfall. On the other hand, when PV production exceeds demand, the surplus is allocated to the subsystems involved in hydrogen and ammonia production, following a predefined prioritization hierarchy. If a battery is present, it is charged and discharged with priority over the chemical storage systems.

A dynamic control variable, denoted as quota (ranging from 0 to 1), determines the fraction of residual renewable energy directed to the chemical storage system that is allocated to the PEMEL. The remaining energy is then distributed among the PSA unit, the ASR, and the hydrogen buffer compressor (if hydrogen storage is required). The energy allocation algorithm that governs the computation of the quota is designed to meet the following objectives:

- Maximize hydrogen production from the PEMEL,
- Ensure continuous operation of the ASR at no less than its minimum load,
- Adjust PSA operation to match the ASR load,
- Ensure total energy consumption does not exceed the available renewable supply.

Depending on hydrogen availability and renewable energy input, the ASR operates under one of the following scenarios:

1. The PEMEL alone generates sufficient hydrogen to meet or exceed the ASR minimum load requirements. The ASR load is then controlled by the most restrictive of the following factors: Hydrogen availability, nominal production capacity, ramp-rate constraints, or any additional load control strategy. ASR operation can either proceed without active control, consuming all the hydrogen directly supplied by the electrolyzer, or under a control strategy that utilizes the level of charge of the hydrogen buffer as an indicator of PV energy availability. If the control strategy is activated, when the buffer LOC drops below a predefined

threshold, the ASR is constrained to operate at minimum load. This approach reduces hydrogen consumption and prioritizes hydrogen accumulation in the buffer under periods of limited PV generation

The hydrogen buffer remains idle in this scenario. If the PEMEL generates more hydrogen than is required by the ASR, the excess is compressed and stored in the buffer, resulting in additional energy consumption due to compression.

2. The hydrogen production by the PEMEL is insufficient to sustain the ASR minimum load, as dictated by operational constraints such as minimum load thresholds or ramp-rate limitations, but the buffer can compensate for the deficit. The ASR is therefore operated at its minimum feasible load

3. Neither the PEMEL nor the hydrogen buffer can supply the minimum required hydrogen flow to maintain ASR operation at its allowable minimum load. As a result, the ASR cannot be operated, and ammonia production is set to zero.

4. Even with the PEMEL off (quota = 0) the renewable supply cannot sustain minimum ASR and PSA operation, and ammonia production is set to zero

The value of quota is determined by numerically solving the energy balance equation, which equates the available renewable energy and the system total energy consumption using Brent's method. The energy allocation algorithm returns the quota, the corresponding ammonia production, and the amount of hydrogen withdrawn from the buffer. These quantities form the basis for calculating electricity consumption across the system components.

Since the ASR cannot shut down, if ammonia production results zero from the energy allocation algorithm or renewable energy is unavailable, the system resorts to a fallback operational mode, as outlined in Fig. 7. In this mode, if the hydrogen buffer contains sufficient reserves, the additional required energy is supplied by the CCGT to maintain ASR operation. Conversely, if the stored hydrogen is insufficient to sustain ASR operation, the system considers the current solution infeasible, indicating that the proposed sizing is not valid.

If the system is hydrogen-based, power allocation is managed by balancing the surplus renewable energy between the electrolyzer and the compressor.

Fig. 8 provides a clear baseline by illustrating the operational dynamics of the two systems with chemical storage only (base case, without battery), showing the temporal evolution of electricity flows and tank storage levels for selected scenarios. The top part displays results for the hydrogen–based system, comprising a 55 MW PV, a 30 MW PEMEL and an H_2 tank with a capacity of 350 t. The bottom part depicts an ammonia-based configuration with a 65 MW PV system, a 35 MW PEMEL, an H_2 buffer with a capacity of 215 t, an ASR with nominal ammonia production of 0.49 kg/s, and an NH_3 tank with a capacity of 1400 t.

The bars represent hourly power flows associated with each technology, while the lines represent the level of charge (in %) of the hydrogen tank in the hydrogen-based system and both the hydrogen buffer and ammonia tank in the ammonia-based system. Two weeks taken as an example are shown, one in July and one in December.

PV generation typically meets the whole electricity demand during daylight hours, with surplus energy used to power the electrolyzer and compressor and also the PSA and ASR in the ammonia-based system, thus contributing to the creation of daily storage of hydrogen and ammonia. However, the shorter daylight periods in winter constrain the effectiveness of daily storage alone, thereby necessitating seasonal storage to guarantee energy availability during the most critical months. Indeed, the limited PV surplus in winter makes summer the main season for energy accumulation. This is evident from the LOC of the storage tanks: during summer the tanks are predominantly charging, whereas in winter a gradual discharge takes place. Additionally, a daily charge–discharge cycle between daytime and nighttime is also observable. At night, the CCGT operates by burning hydrogen or ammonia to meet the electricity demand. In the ammonia-based configuration, CCGT also supplies energy to the PSA and ASR units during nighttime hours.

2.12. Case studies and sizing approach

To assess the relative advantages of ammonia over hydrogen as an energy storage solution, a base case with only chemical storage is first analyzed, comparing hydrogen and ammonia under a constant electricity demand of 4 MW evenly distributed across all hours of the year. By removing the complexity of multiple storage options and variable demand profiles, this setup isolates systems behavior. Constant demand also reflects real-world applications such as industrial facilities or data centers, which often operate with steady power requirements. Subsequent analyses include sensitivity studies for other demand profiles, and the systems are extended to include a battery for short-term balancing.

The economic parameter adopted for optimizing system sizing is the LCOE defined as the average cost per unit of electricity generated over the lifetime of a power generation system. It represents the minimum electricity selling price required for the project to break even, accounting for both CApital EXpenditures (CAPEX) and OPerational EXpenditures (OPEX). LCOE is calculated by dividing the total discounted costs of the system by the total discounted electricity output over its lifetime:

$$LCOE = \frac{CAPEX + \sum_{j=1}^{n} \frac{\left(\sum_k C_{\mathrm{rep},k,j} + OPEX_j\right)}{(1+i)^j}}{\sum_{j=1}^{n} \frac{E_j}{(1+i)^j}} \tag{7}$$

In this expression j indicates the year index, n is the project lifetime (20 years in this study), i is the discount rate (in this case the Weighted Average Cost of Capital, WACC, is used), E_j is the electricity consumption in year j, $C_{\mathrm{rep},k,j}$ is the replacement cost of component k in year j, and $OPEX_j$ is the operating expenditure in year j.

Comprehensive economic calculations and the associated parameters and component costs are provided in the Supplementary Information (Section S6).

When storage is implemented in the form of ammonia, the sizing parameters include the photovoltaic plant capacity, the electrolyzer capacity, the hydrogen buffer size, the ammonia synthesis reactor size, and the NH_3 tank size. The number of PSA units is determined based on the ammonia synthesis reactor capacity, with each unit sized at 400 Nm^3/h of nitrogen, corresponding to the largest commercially available unit for the required purity. The combined cycle gas turbine is initially assigned an oversized capacity, which is subsequently reduced based on the maximum electrical demand recorded during simulation. Since the reactor cannot be turned off, any excess ammonia produced when the NH_3 tank is full is discarded.

When hydrogen is used as the storage medium, the sizing variables are limited to PV capacity, electrolyzer capacity, and hydrogen tank size. Here, the CCGT capacity is set equal to the maximum electrical demand.

In the extended systems with a battery, its size is fixed at an 8-hour nominal duration.

The optimization problem is solved using a Bayesian optimization algorithm [74,75] based on the Tree-structured Parzen Estimator method [76]. The objective function (i.e. the LCOE) is evaluated through system simulations: for each set of design variables, a full-plant simulation is performed to assess technical feasibility. Several penalization rules are introduced to exclude physically or operationally unrealistic solutions, specifically:

1. The electrolyzer capacity must not exceed the installed PV plant capacity minus minimum electricity demand.
2. The storage tank level at the end of the simulation year must be equal to or greater than the initial level, to avoid artificially "creating" hydrogen or ammonia.
3. No electricity can be imported from the grid.
4. The ammonia synthesis reactor must operate continuously, at least at its minimum load, and within ramp-rate constraints.

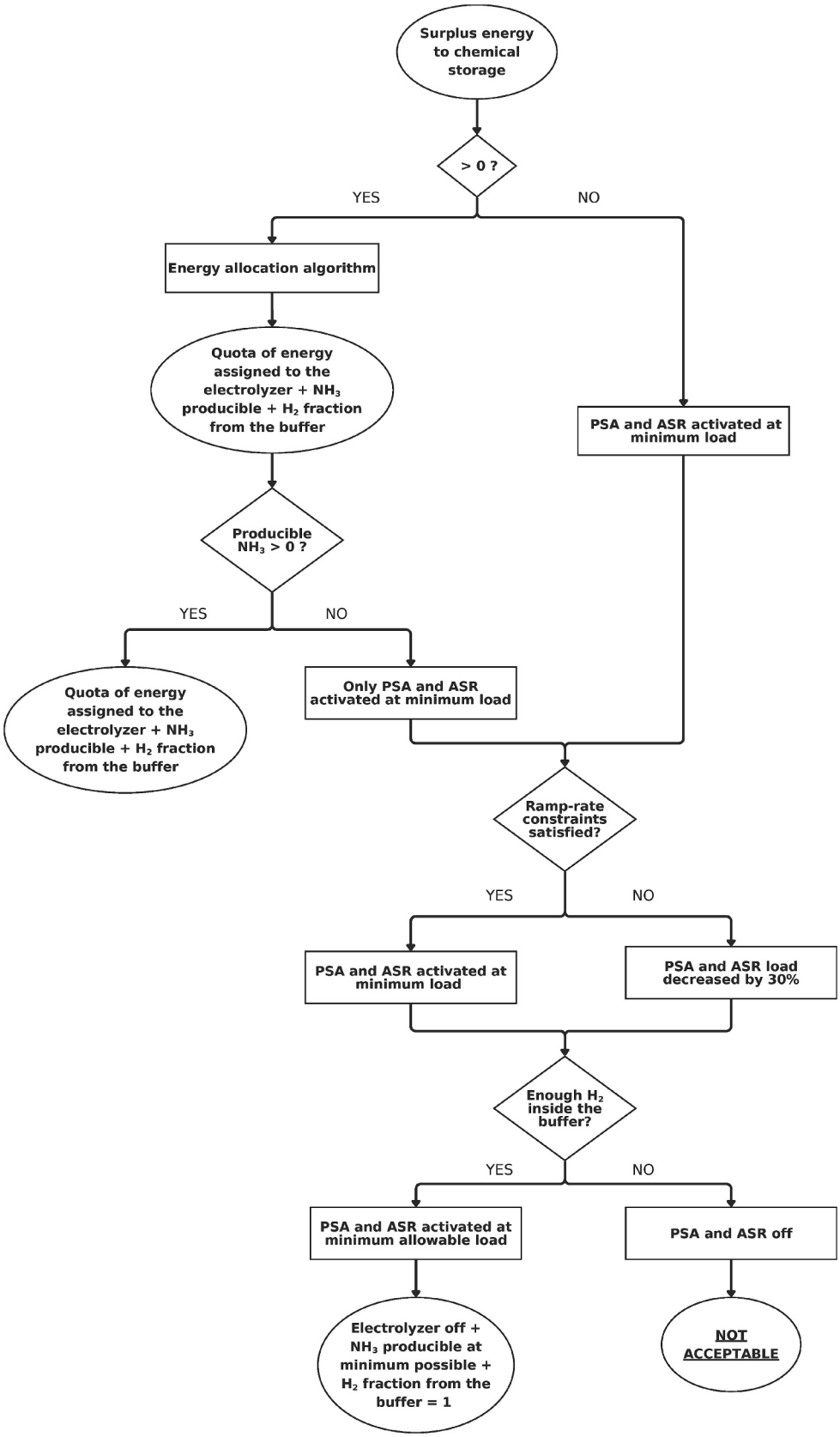

Fig. 7. Workflow of components operation and energy allocation from surplus renewable energy directed to chemical storage – ammonia-based system.

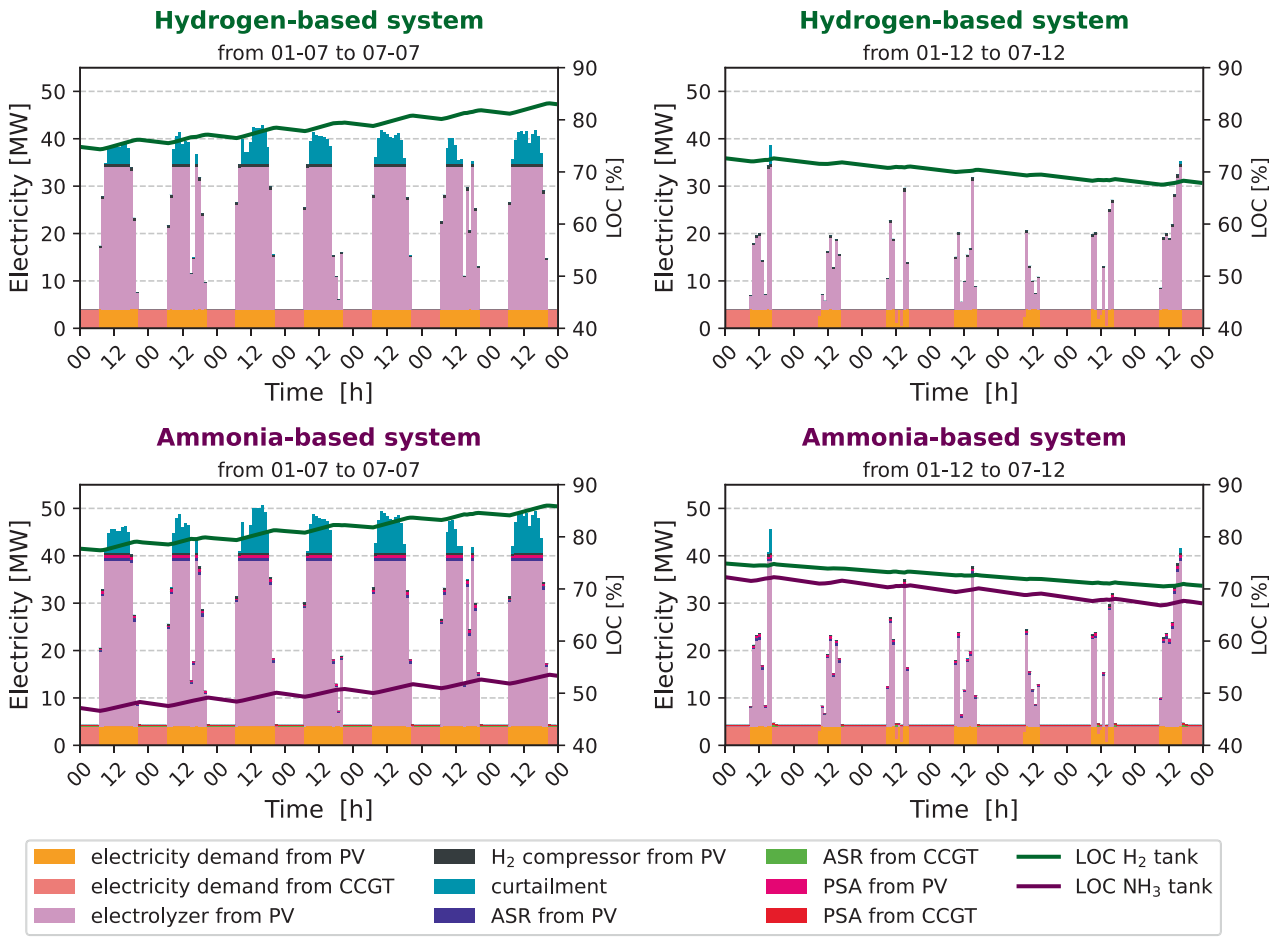

Fig. 8. Hourly electricity balances (bars) and tanks LOC (lines) over one week in December (left) and July (right); hydrogen-based case (top) and ammonia-based case (bottom).

If any of these constraints are violated, the solution is deemed infeasible and is penalized by assigning a very large objective function value.

The range of sizing variables considered for LCOE optimization is reported in Table 2. The minimum PV capacity was set to ensure the constant 4 MW demand could be met at a 20 % capacity factor, while the maximum value was chosen to reflect a realistic upper limit. The ranges for the remaining variables were defined through preliminary simulations to identify feasible equipment sizes for the system.

Another parameter used to interpret the results is the Levelized Cost of Storage (LCOS), that expresses the total lifetime cost of a storage system as an equivalent cost per unit of electricity discharged. LCOS calculation follows the same formula as the LCOE but replaces total system costs with only the CAPEX, OPEX, and replacement costs of the storage system components, and considers only the electricity generated from stored hydrogen or ammonia in the CCGT to satisfy the electricity demand [77]. For the hydrogen-based system, the storage system components are the hydrogen compressor, H_2 tank, and CCGT; for the ammonia-based system, they include the hydrogen compressor, hydrogen buffer, ASR, PSA, NH_3 tank and CCGT. In the battery-integrated case, the battery is included among the storage system components for the LCOS calculation, and the electricity discharged from the battery is added to that generated by the CCGT in the LCOS denominator.

Table 2
Input variable ranges considered in LCOE optimization.

Component	Ammonia-based system	Hydrogen-based system
PV	20–150 MW	20–150 MW
PEMEL	1–150 MW	1–150 MW
H_2 tank	1–300 t	15–1000 t
ASR	0.1–1.0 kg/s	–
NH_3 tank	100–4000 t	–

3. Results and discussion

This section presents the sizing and LCOE results of the case studies optimizations, followed by an analysis and comparison of ammonia-based and hydrogen-based systems. First, the base case for both systems, relying solely on chemical energy storage, is considered with a constant demand profile, providing a clear view of the systems dynamics. Next, a sensitivity analysis is performed on the base case by varying the demand profile throughout the year while keeping the total energy demand constant, in order to assess the impact of demand variability. Finally, a case with integrated battery storage is examined to evaluate its effect on energy management and the economic performance of the systems.

3.1. Base case – constant demand profile

The results for both systems for the base case without battery and constant 4 MW demand scenario are presented in two stages.

First, an analysis of LCOE maps generated across a wide range of component sizes identifies cost–optimal regions and assesses the sensitivity to variations in PV, electrolyzer, storage, and ammonia synthesis reactor capacities.

Then, optimal results are discussed in greater detail. In particular, two operational strategies are evaluated for the ammonia-based system. The first employs the rule-based approach without any active control over the ammonia synthesis reactor, allowing it to operate with all the possible hydrogen available from the electrolyzer. The second introduces a control strategy designed to curtail ASR operation during specific unfavorable periods, such as when hydrogen availability inside the buffer is low.

3.1.1. LCOE maps

Fig. 9 and Fig. 10 display the LCOE maps for the hydrogen-based and ammonia-based systems, respectively. For the hydrogen-based system, the explored variables are H_2 tank size, electrolyzer size, and PV size, while for the ammonia-based system the ASR size is also included·NH_3 tank size is not treated as a variable in the maps; instead, its optimized value is used (that is the minimum size required for a given ASR, PV, electrolyzer, and buffer capacity). This choice reflects its reduced impact on LCOE compared to the other variables.

The regions where no LCOE values are indicated correspond to scenarios where a solution can't be identified. Specifically, these are areas where the system cannot operate in an islanded mode, or in the case of the ammonia-based system, also configurations where the ASR turns off.

In the hydrogen-based configuration, larger PV capacities combined with correspondingly sized electrolyzers ensure a stable energy supply and consistent hydrogen production throughout the year. This design approach minimizes reliance on large-scale seasonal storage, allowing the system to operate primarily with short-term buffering. In contrast, smaller PV systems necessitate larger hydrogen tanks to offset seasonal energy shortages and the associated drop in hydrogen production. Among all configurations, the lowest LCOE values are observed with oversized PV fields and minimal storage capacity, reflecting the high costs associated with long-term hydrogen storage.

The ammonia-based configuration exhibits similar cost trends due to the presence of the hydrogen buffer. When ammonia is employed as the energy storage vector, the main limitation of the ASR lies in its limited flexibility to respond to PV generation variability, primarily due to constraints on shutdowns. To ensure adequate hydrogen availability within the buffer during the winter months for continuous ammonia synthesis, it is economically advantageous to oversize the PV system. This enables the system to rely primarily on short-term hydrogen buffering, avoiding costly seasonal hydrogen storage. Again, the most favorable LCOE outcomes are found in configurations with large PV systems and minimal hydrogen buffer capacity. ASR sizing also plays a critical role. Smaller ammonia synthesis reactors yield the lowest LCOE, as their lower hydrogen demand reduces hydrogen storage needs. While this requires a higher PV size to compensate for the lower ammonia production capacity, the reduction in hydrogen buffer size offsets the higher PV cost. Increasing the ASR size introduces greater operational flexibility by enabling more extensive ammonia storage to bridge periods of low renewable energy availability. This flexibility allows for a moderate reduction in PV capacity. However, the higher minimum operating load of the ASR increases the hydrogen buffer requirement, leading to a net rise in LCOE. For the largest ASR size considered, the reactor high minimum load mandates a consistent hydrogen supply throughout the year. This necessitates both larger generation and buffer capacities. Additionally, during periods of high renewable availability, the ASR may produce excess ammonia relative to demand.

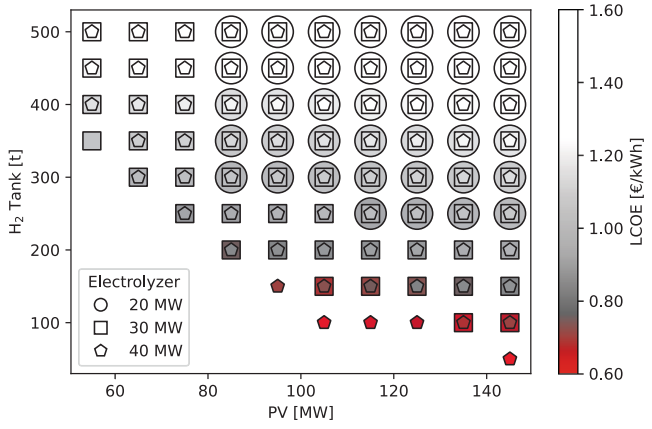

Fig. 9. LCOE map for the hydrogen-based system as a function of PV size (x-axis), hydrogen tank size (y-axis), and electrolyzer size (marker shape). LCOE values are represented by the colormap.

Fig. 9 and Fig. 10 also highlight that the sizing of the electrolyzer coupled with the PV size affects the feasibility of the solutions. With a fixed hydrogen storage capacity, increasing the electrolyzer size can allow for a reduction in PV size: although a smaller PV system results in lower energy availability, a larger electrolyzer can achieve a hydrogen production level comparable to that of a larger PV system coupled with a smaller electrolyzer. At high PV capacities, increasing electrolyzer size allows more efficient use of winter surplus, reducing the required seasonal storage volume.

3.1.2. Optimization results

The optimal system configurations resulting from the LCOE minimization are summarized in Table 3.

In the hydrogen-based scenario, the optimization yields a trade-off between PV oversizing and the use of the hydrogen storage tank for seasonal energy balancing, with a 120 MW PV, a 40 MW PEMEL, and an H_2 tank with a capacity of 63 t. Rather than maximizing the PV capacity up to the imposed limit (150 MW), the economic optimization identifies an intermediate solution that reduces excessive hydrogen storage requirements while avoiding unnecessary PV oversizing. The resulting LCOE is 0.575 €/kWh.

For the ammonia-based system, the ASR is initially assumed to operate according to a rule–based, uncontrolled strategy. Even in this case, the installed PV capacity remains below the maximum allowable threshold, reaching a size of 120 MW as in the hydrogen-based case. The electrolyzer is accordingly sized at 34 MW, while the ammonia synthesis reactor is dimensioned at 0.44 kg/s with 3 PSA units, resulting in a tank sizing of 1210 t to ensure ammonia availability during low PV generation periods. Despite PV oversizing, a substantial hydrogen buffer of 28 t is still required. The resulting LCOE is 0.592 €/kWh.

Fig. 11 presents the monthly electricity and hydrogen balances, broken down by the contribution of each system component. In the electricity balance, positive values represent electricity production (from the PV and CCGT), while negative values correspond to electricity consumption (from the electricity demand, ASR, PSA, and electrolyzer), with curtailment also included in the negative values. In the hydrogen balance, positive values indicate hydrogen production by the electrolyzer and discharging from the hydrogen tank, while negative values represent hydrogen consumption by the ASR in the ammonia-based system or by the CCGT in the hydrogen-based system. Additionally, negative values for the tank correspond to hydrogen charging.

The hydrogen balances in Fig. 11 clearly highlight that both the hydrogen-based and ammonia–based systems tend to produce and store a significant amount of hydrogen even during the winter months. This behavior is more pronounced in the hydrogen-based system, where hydrogen production is even reduced during the summer. Conversely, the ammonia-based system exhibits a more uniform hydrogen production profile throughout the year, with a slight increase observed during the summer period. In both cases, as can be seen from the electricity balances in Fig. 11, substantial share of surplus photovoltaic energy remains unutilized during the summer months.

The difference in hydrogen production trends between the two systems highlights the more pronounced seasonality associated with ammonia-based storage.

In the hydrogen-based configuration, the system adopts a

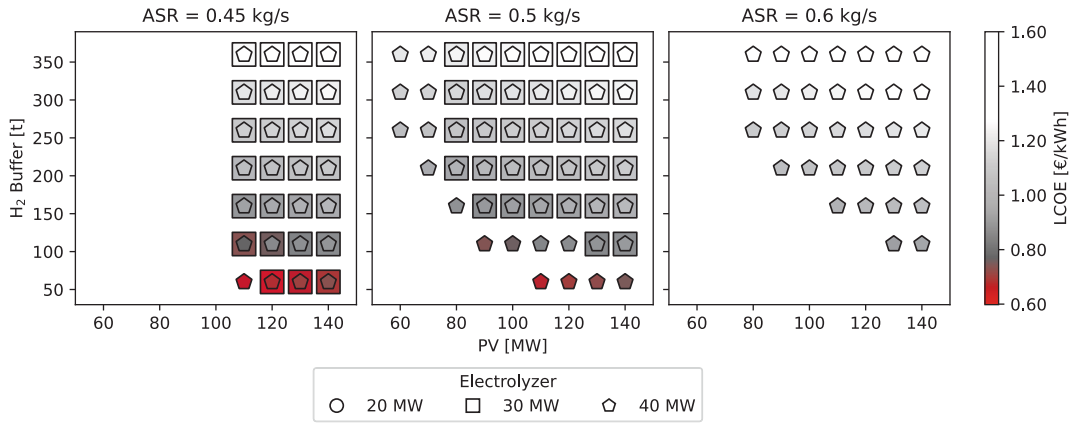

Fig. 10. LCOE map for the ammonia-based system at three ASR sizes, as a function of PV size (x-axis), hydrogen tank size (y-axis), and electrolyzer size (marker shape). LCOE values are indicated by the colormap.

Table 3
Sizing results obtained with LCOE minimization.

Component	Hydrogen-based system	Ammonia-based system without ASR control	Ammonia-based system with ASR control
PV [MW]	120	120	96
PEMEL [MW]	40	34	30
H_2 Tank [t]	63	28	23
PSA [n°]	–	3	3
ASR [kg/s]	–	0.44	0.50
NH_3 Tank [t]	–	1210	1660
CCGT [MW]	4	4.75	4.65
LCOE [€/kWh]	0.575	0.592	**0.529**

predominantly short-term storage strategy. During summer, hydrogen production is intentionally curtailed, even though both the electrolyzer and PV system are sized for high output. This approach is visible in the hydrogen tank level of charge profile shown in Fig. 12: the LOC frequently approaches its upper limit during summer, forcing the electrolyzer into partial load or shutdowns. Furthermore, during the initial winter months of the year, the tank does not exhibit the expected depletion typical of systems relying on seasonal storage. On the contrary, the LOC continues to rise, and the tank reaches full capacity as early as March. A complete discharge of the tank occurs only in November and December, coinciding with the period of lowest solar energy availability.

In contrast, the ammonia-based system exhibits a more clearly seasonal ammonia storage behavior. All the ammonia produced by the reactor is stored in the NH_3 tank, without losses. The ASR produces more ammonia during the summer, anticipating winter demand, as evidenced by the ASR hydrogen consumption trend in Fig. 11 and by the ammonia tank LOC profile in Fig. 12. This is possible because the relatively low cost of the ammonia tank allows full exploitation of reactor production without oversizing it for short-term storage. Nevertheless, the LOC of the hydrogen buffer follows the same trend as the hydrogen tank in the hydrogen-based case. However, in the ammonia-based case, the relatively high hydrogen production observed during winter is primarily driven by the need to maintain continuous ASR operation, rather than by

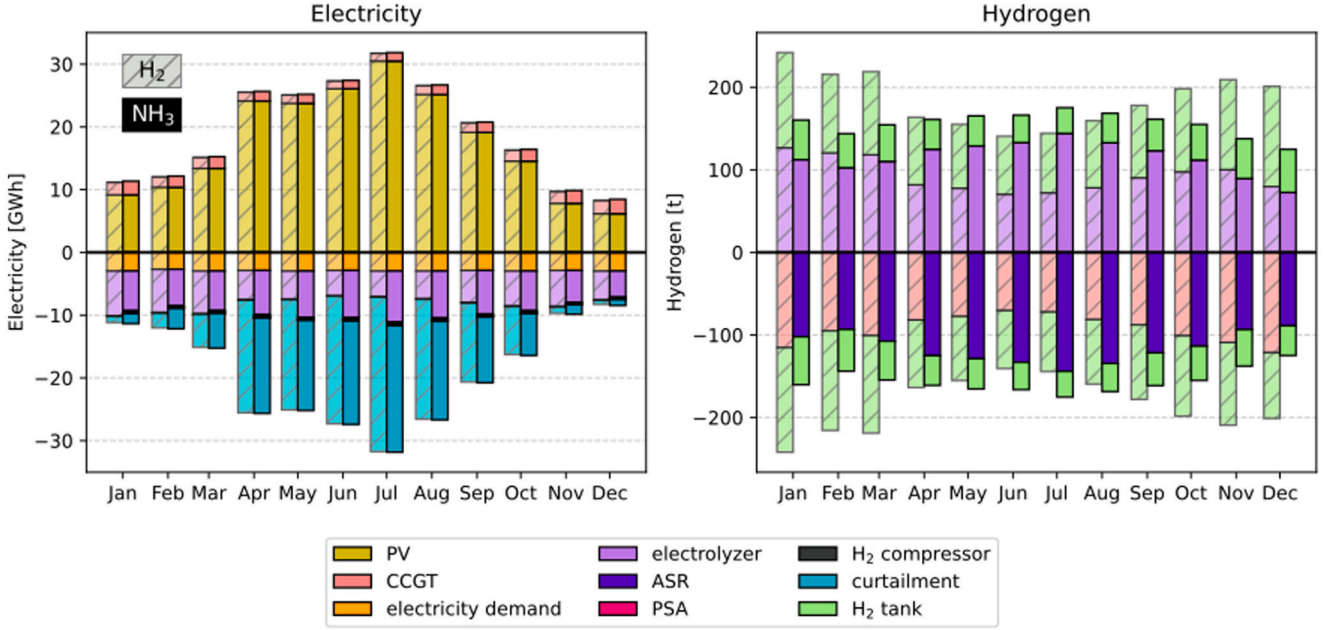

Fig. 11. Monthly electricity and hydrogen balances, broken down by component contributions. For each month, the bars on the left represent the hydrogen-based case (hatched and semi-transparent), while the bars on the right represent the ammonia-based case (solid fill).

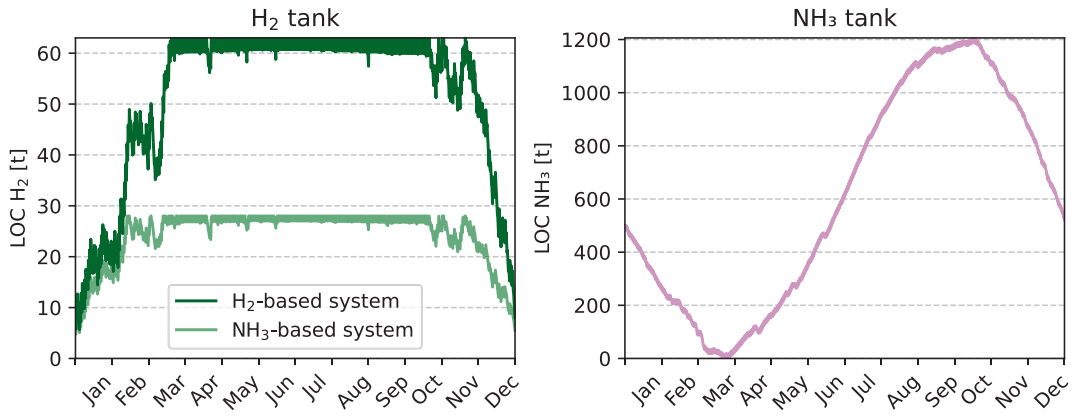

Fig. 12. Tanks level of charge over the year. The left plot shows the hydrogen tank LOC for both systems; the right plot shows the ammonia tank LOC for the ammonia-based system.

an intentional strategy for short-term balancing during periods of low PV availability. A portion of ammonia storage is also used for daily balancing during winter, particularly under uncontrolled reactor conditions, where the system lacks the ability to modulate ASR load in response to varying PV availability.

The ammonia-based configuration does not yield a cost advantage, since the additional capital and operational costs associated with the ammonia synthesis reactor, PSA units, and ammonia tank offset savings from smaller hydrogen storage and electrolyzer size. Moreover, the PV system remains significantly oversized at 120 MW (same as the hydrogen-based case), as the need to continuously supply hydrogen to the ammonia synthesis reactor forces overproduction even during periods of low solar irradiance. The LCOS, which measures the cost of storing energy, highlights the added storage system cost for the ammonia-based case with a value of 0.377 €/kWh versus 0.311 €/kWh for the hydrogen–based case. Despite the lower electrolyzer size and the same PV size, ammonia storage proves less cost-effective than direct hydrogen storage due to the higher LCOS.

To improve the management of the hydrogen buffer, a load control strategy is implemented for the ASR in the ammonia-based system. This approach modulates the ASR load based on the level of charge of the hydrogen buffer, which serves as an indicator of PV energy availability. When the LOC falls below a predefined threshold, the ASR is forced to operate at minimum load, thereby reducing hydrogen consumption and

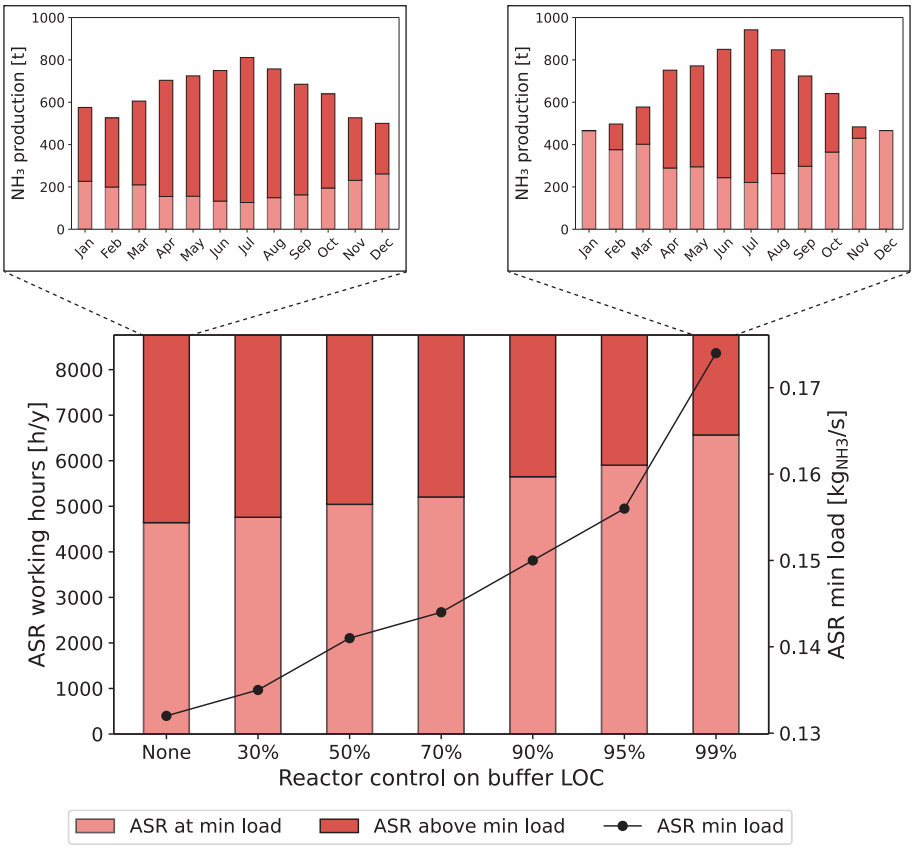

Fig. 13. ASR operating hours at minimum load or above minimum load (bars) and corresponding reactor minimum load (points) for different reactor control strategies. A zoomed-in view for two selected control cases highlights the ammonia production throughout the year, distinguishing between production at minimum load and above minimum load.

prioritizing its accumulation in the buffer. This contrasts with the rule-based baseline strategy, where the ammonia synthesis reactor consumes all the available hydrogen from the electrolyzer within its operational capacity immediately converting it into ammonia, regardless of storage considerations. This would either require oversizing hydrogen production beyond the ASR absorption capacity during energy–scarce periods or increasing seasonal hydrogen storage to ensure continuous reactor operation.

The system is evaluated under several LOC thresholds: 30 %, 50 %, 70 %, 90 %, 95 %, and 99 %. The impact of this control strategy on ammonia production is illustrated in Fig. 13. Higher thresholds result in a noticeable reduction in ammonia output during winter, as the ASR works more hours at minimum load.

Introducing ASR control significantly alters system sizing and energy flows. By limiting hydrogen consumption to the minimum required to maintain the ammonia synthesis reactor minimum load during periods of low PV availability and storing the surplus, there is a notable reduction in the required capacity of the hydrogen buffer, electrolyzer, and PV system, as illustrated in Fig. 14. However, this control strategy leads to reduced ammonia output during periods of low renewable generation, introducing a seasonal production imbalance. To compensate, the ASR must be upsized, allowing for increased ammonia synthesis during periods of high PV availability. Fig. 15(a) illustrates the monthly percentage differences in ammonia production relative to the uncontrolled baseline. As the control level increases, the system gradually shifts toward a more seasonal production profile: more ammonia is produced and stored during the summer, while winter sees reduced production and greater reliance on stored ammonia. This results in progressively higher mid-year peaks and lower values at the beginning and end of the year in the production curves.

A closer analysis of the optimized system sizing and ammonia production over the year reveals important dynamics. When the ASR load is controlled to operate at minimum load when the hydrogen buffer LOC drops below 30 %, the reduction in the size of the PV and electrolyzer is modest. In fact, as shown in Fig. 15(a), ammonia production remains almost unchanged, with only slight reductions in January and December. As the control range widens to 50–70 % of the LOC, the hydrogen buffer size also decreases. This is due to reduced ammonia production during a broader portion of the winter, particularly in December, while summer production increases significantly, reinforcing the seasonal production pattern as shown in Fig. 15(a). When the control threshold is raised further to 90 % of the LOC, a notable shift occurs. Although the seasonal production behavior becomes more pronounced, the buffer size increases again, indicating a renewed reliance on seasonal hydrogen storage. In fact, despite the ASR operating always at minimum load in December (Fig. 15(b)), ammonia production increases compared to the 50–70 % control cases (Fig. 15(a)) as the increased ASR size required to meet the tighter control constraint leads to a higher minimum load. This excessive hydrogen consumption in December brings the system back to a higher need for seasonal hydrogen storage. In the 95 % and 99 % control scenarios, this effect intensifies. Furthermore, in the 99 % control scenario, the production curve rises again in the winter months and stays flat or slightly lower in summer compared to the 95 % case. For instance, ammonia production in November is significantly higher than in the 90 % case, even though the ASR does not run at minimum load for the entire month (Fig. 15(b)). This behavior indicates that in this case the ASR oversizing is not a strategic design choice to support seasonal ammonia storage, but becomes rather a compensatory measure to meet tight operational constraints. The system must increase the minimum production value, and the only feasible way is by installing a larger reactor.

As a result, when the control threshold exceeds 90 %, the sizes of the electrolyzer, PV system, and hydrogen buffer begin to increase again alongside the ASR size, as shown in Fig. 14.

This excessive control undermines the system seasonal ammonia storage strategy and ultimately results in poorer economic performance compared to lower control levels, causing a minimum in the LCOE curve. This trend is evident in Fig. 16, which reports the resulting LCOE for different control strategies.

From an economic perspective, the optimal trade-off between component sizes is achieved when the ASR is controlled at 90 % of the hydrogen buffer capacity. As the control level increases up to 90 %, the LCOE contributions from the PV system and electrolyzer consistently decrease. The hydrogen buffer, instead, reaches its minimum cost contribution at around 70 % control. Nevertheless, the total system LCOE continues to decline up to 90 % control, since the additional investment in the ammonia synthesis reactor, pressure swing adsorption unit, and ammonia tank remains relatively modest compared to the significant savings enabled by downsizing the more capital-intensive components. The lowest LCOE achieved is 0.529 €/kWh, making the ammonia-based system more cost-effective than the hydrogen–based configuration, which reaches 0.575 €/kWh.

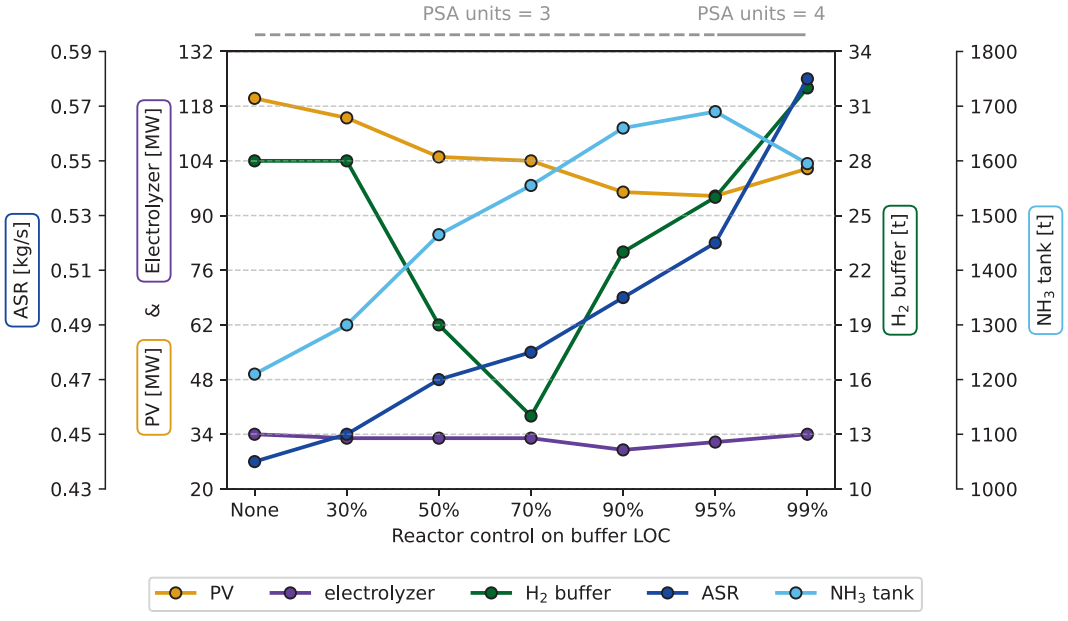

Fig. 14. Impact of hydrogen buffer control thresholds on component sizing in the ammonia-based system, based on LCOE optimization.

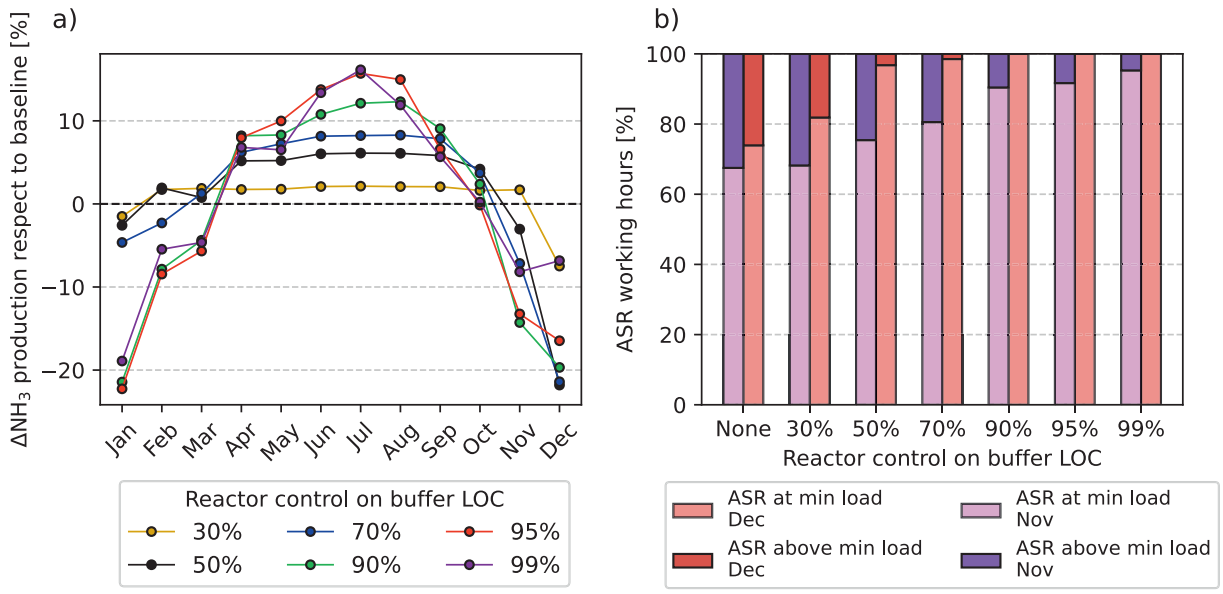

Fig. 15. A) monthly percentage differences in ammonia production for different reactor control strategies, compared to the uncontrolled baseline case. b) asr working hours at minimum load in november and december for different reactor control cases.

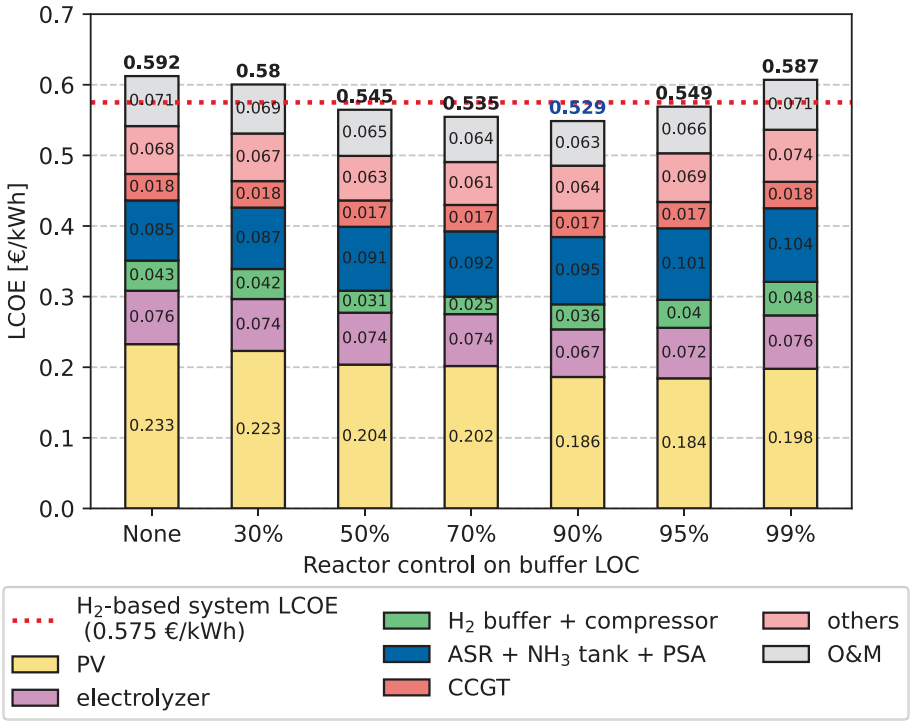

Fig. 16. Impact of hydrogen buffer control thresholds on LCOE in the ammonia-based system.

When optimally tuned, the ASR control strategy not only improves the utilization of surplus renewable energy by shifting ammonia production to periods of high PV generation but, more importantly for the economic analysis, enhances the overall cost-efficiency of the ammonia-based system.

When the LCOS for the ammonia-based system is evaluated with reactor control at 90 % of the buffer LOC, it remains at 0.377 €/kWh. However, the possibility of reducing the size and thus the cost of both the PV and the electrolyzer, as shown in Fig. 17, makes ammonia more cost-effective. This benefit stands in contrast with the dynamics observed in hydrogen-based system sizing, where attempts to reduce the tank cost lead to significantly larger photovoltaic and electrolyzer capacities.

3.2. *Base case – sensitivity analysis on the electricity demand profile*

To gain deeper insight into the advantages of ammonia as a renewable energy storage solution, it is essential to explore variations of the load profile. By analyzing extreme scenarios, it becomes easier to identify the conditions under which ammonia-based storage becomes particularly advantageous. In this context, two additional load profile scenarios are considered: one featuring a peak in electricity demand

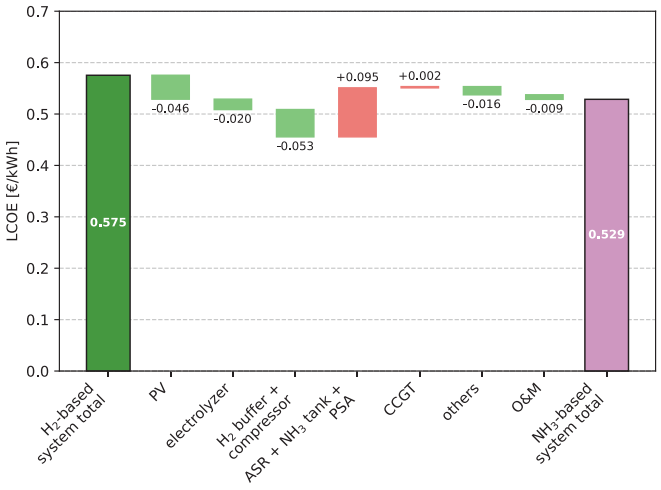

Fig. 17. Waterfall chart showing the LCOE difference between NH_3-based system (with reactor control on 90% buffer LOC) and H_2-based systems, with incremental cost impacts of each component.

during the summer months, and another with a peak in the winter months (Fig. 18). Both profiles are designed to have the same total annual energy demand as the constant demand case, ensuring a fair comparison focused only on the temporal distribution of energy needs.

The optimized ammonia synthesis reactor control strategy (reactor curtailed when hydrogen buffer LOC < 90 %) is applied to all scenarios. Fig. 19 presents a comparison of components sizing and resulting LCOE values across the three load profiles. In the ammonia-based system, the combined contribution of the ASR, PSA, and NH_3 tank are shown together to highlight the difference relative to the hydrogen-based case. For more detail, in the constant-demand case the NH_3 tank accounts for about 22 % of this contribution, the ASR for 62 %, and the remainder for the PSA. In the summer-peaked case the NH_3 tank contributes 10 %, the ASR 71.5 %, and the rest is PSA. In the winter-peaked case the NH_3 tank represents 48 %, the ASR 37 %, and the balance is PSA.

The results confirm that the shape of the load profile strongly influences which storage solution is more cost-effective.

The low cost of ammonia storage tanks, around 5 €/kg_{NH3} (0.96 €/kWh), makes ammonia suitable for large-scale, long-duration energy storage. In the constant demand case, although the LCOS of the ammonia-based case is higher than that of the hydrogen-based case, the low tank cost per kWh of stored energy allows economically favorable sizing with smaller PV and electrolyzer, relying more on seasonal storage than the hydrogen-based system.

The advantage of using ammonia for long-term storage becomes evident in the winter-peaked scenario, where the LCOE with ammonia storage is 0.666 €/kWh, compared to 1.209 €/kWh for hydrogen. In the hydrogen-based system the high cost of storage tanks, approximately 470 €/kg_{H2} (~14 €/kWh), accounts for nearly 30 % of the total LCOE, significantly impacting both capital and operating costs. The LCOS highlights this difference, with hydrogen at 1.101 €/kWh and ammonia at 0.472 €/kWh, showing that both PV and electrolyzer downsizing and the much lower storage system costs drive ammonia advantage.

By contrast, under a summer-peaked load profile, where short-term storage is the dominant requirement, hydrogen becomes advantageous, achieving an LCOE of 0.343 €/kWh compared to 0.483 €/kWh for ammonia. This cost advantage is mainly due to the alignment between energy demand and solar availability. With reduced storage needs, the hydrogen-based system avoids the oversizing seen in other scenarios, allowing smaller upstream components and improving overall cost efficiency. The LCOS for the ammonia-based systems is 0.377 €/kWh compared to 0.239 €/kWh for the hydrogen–based case, with PV and electrolyzer capacities also larger in the ammonia-based case. This results from operational constraints such as limited flexibility in ASR shutdown, ramp-rate restrictions, and lower round-trip efficiency, that arise particularly in short–term storage. As storage duration decreases, the dominant cost drivers shift from storage tanks to the equipment required to produce the storage medium, reducing the economic advantage of ammonia.

Although ammonia production and storage volumes vary significantly across scenarios, the overall system cost remains relatively stable. This is largely due to the low cost of the ammonia tank, the nearly uniform monthly production profile that supports seasonal accumulation (as shown in Fig. 20), and the reduced variation in upstream system sizes. The ammonia system limited flexibility prevents it from fully exploiting reduced storage needs, and thus from achieving the same degree of cost reduction in the summer-peaked scenario as the more adaptable hydrogen system.

On the other hand, the LCOE of the hydrogen system varies considerably across different scenarios due to its high sensitivity to storage capacity. Even small changes in required storage volume cause substantial cost swings (Fig. 19). To manage this, the hydrogen system relies on oversizing upstream components, namely the PV array and electrolyzer. This helps align production with demand and reduces reliance on storage, as shown in Fig. 20. However, the resulting variation in size and cost of upstream components still contributes to overall LCOE instability.

To conclude, ammonia is superior for seasonal storage applications

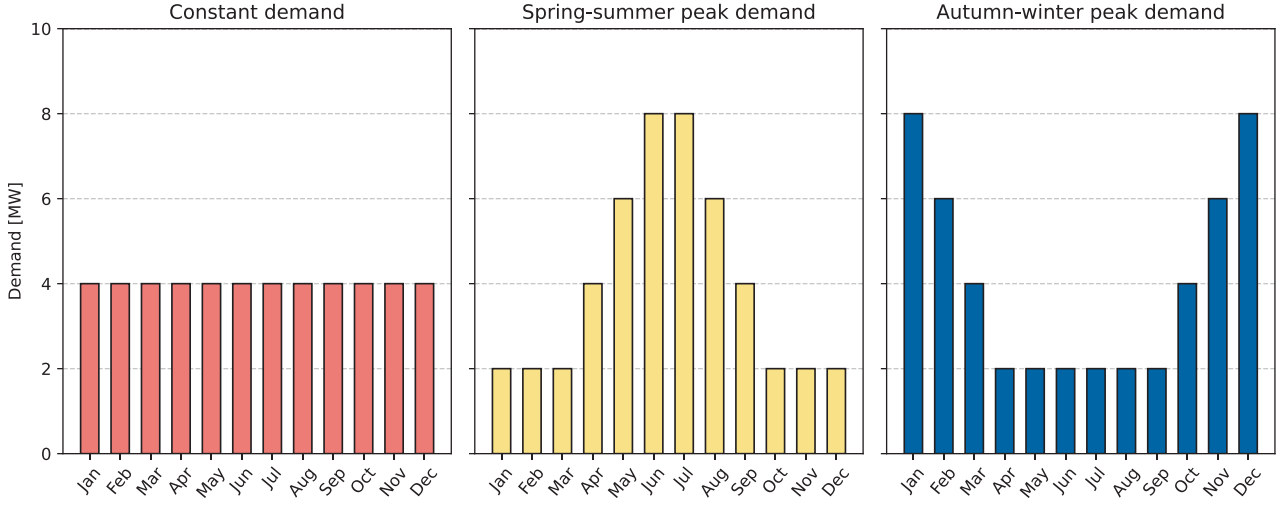

Fig. 18. Electricity demand profiles used in the sensitivity analysis.

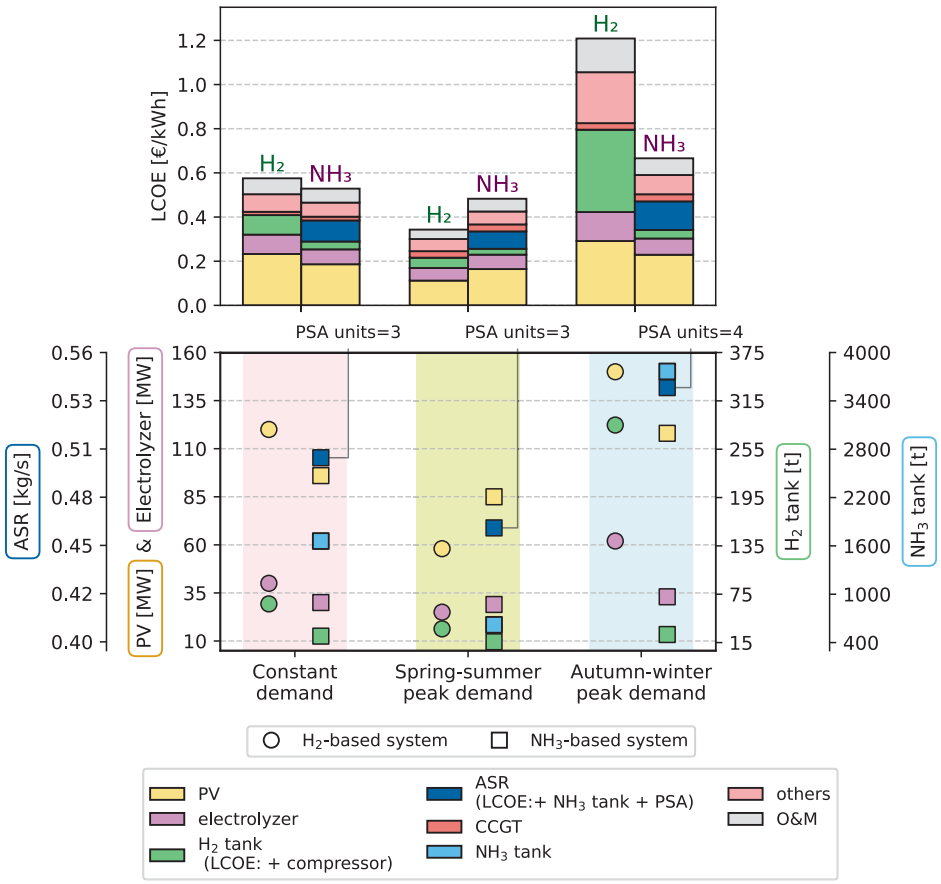

Fig. 19. Results for sensitivity analysis on the electricity demand profile: LCOE at the top and component sizes at the bottom. Colors represent components; markers indicate storage system (circle: hydrogen-based, square: ammonia-based).

due to its low storage cost, which accounts for the entire storage system (PSA + ASR + NH_3 tank), while hydrogen proves more cost–effective when demand aligns with generation, thanks to its higher round–trip efficiency and simpler storage system architecture. In such scenarios, ammonia operational constraints limit its adaptability and economic competitiveness.

3.3. Battery-integrated case

Since batteries are typically used to manage short-term balancing in PV-based systems, a battery storage unit is integrated into the base case systems. The battery has an 8-hour nominal duration, corresponding to 4 MW / 32 MWh in the constant demand scenario, and 8 MW / 64 MWh in the summer–peaked and winter-peaked demand scenarios. For the ammonia-based system, the optimized ammonia synthesis reactor control strategy (on 90 % of the buffer LOC) is applied to all scenarios.

Table 4 reports the results for the demand profile scenarios analyzed in the sensitivity, with old values for the systems without battery and new values for the systems with battery in bold.

As a first step, it is important to see how the battery modifies storage dynamics during the day in different seasons. Fig. 21 reports the average hourly storage rates of ammonia and hydrogen for July and December, representing the most extreme months in terms of PV production. A positive value indicates that H_2 or NH_3 is being stored, while a negative value indicates that it is being discharged.

Thanks to battery integration, in the constant and summer-peaked scenarios in July, the tanks discharge only in the early morning (~4:00–6:00). For the rest of the night, the H_2 storage rate in the H_2–based system remains at zero, while the NH_3 tank in the NH_3–based system shows a positive storage rate, as the reactor continues operating at minimum load. In the winter-peaked scenario, instead, the H_2 tank in the H_2-based system remains idle, since the battery alone can cover the relatively low summer load. The NH_3-based system shows smaller fluctuations in the storage rates but still maintains positive storage rates across the full 24 h, due to continuous reactor operation.

In December, for the constant demand and winter-peaked scenarios, the battery covers the load for a few hours and both systems discharge at similar rates to the case without a battery from midnight until ~ 8:00. In the evening (~16:00–midnight), discharge rates are lower because the battery partly covers demand. The NH_3 system relies more on long-term storage, visible as the absence of positive storage rates during daylight hours. The H_2 system maintains its short–term balancing approach, with sustained positive storage rates during daylight. In the summer-peaked scenario, both systems show reduced fluctuations compared to the case without a battery: low winter demand combined with the battery contribution allows most of the load to be covered without significant use of the chemical storage.

From the sizing results in Table 4 it is clear that almost all components across systems and demand scenarios are reduced in size. PV capacity decreases because the battery higher round-trip efficiency requires less input energy than storing electricity as hydrogen or ammonia. The only exception is the winter-peaked demand scenario for the hydrogen-based system, where reducing the size of the H_2 tank drives again the PV capacity to its maximum, since seasonal storage remains critical for the costs of the H_2-based system. The reduction of components providing production of chemical (hydrogen or ammonia) is explained by the share of energy now stored in the battery. Tank sizes decrease in all scenarios for both systems, except for the ammonia-based system in the summer-peaked scenario. In the constant demand and winter-peaked scenarios, tank size reductions occur because the battery,

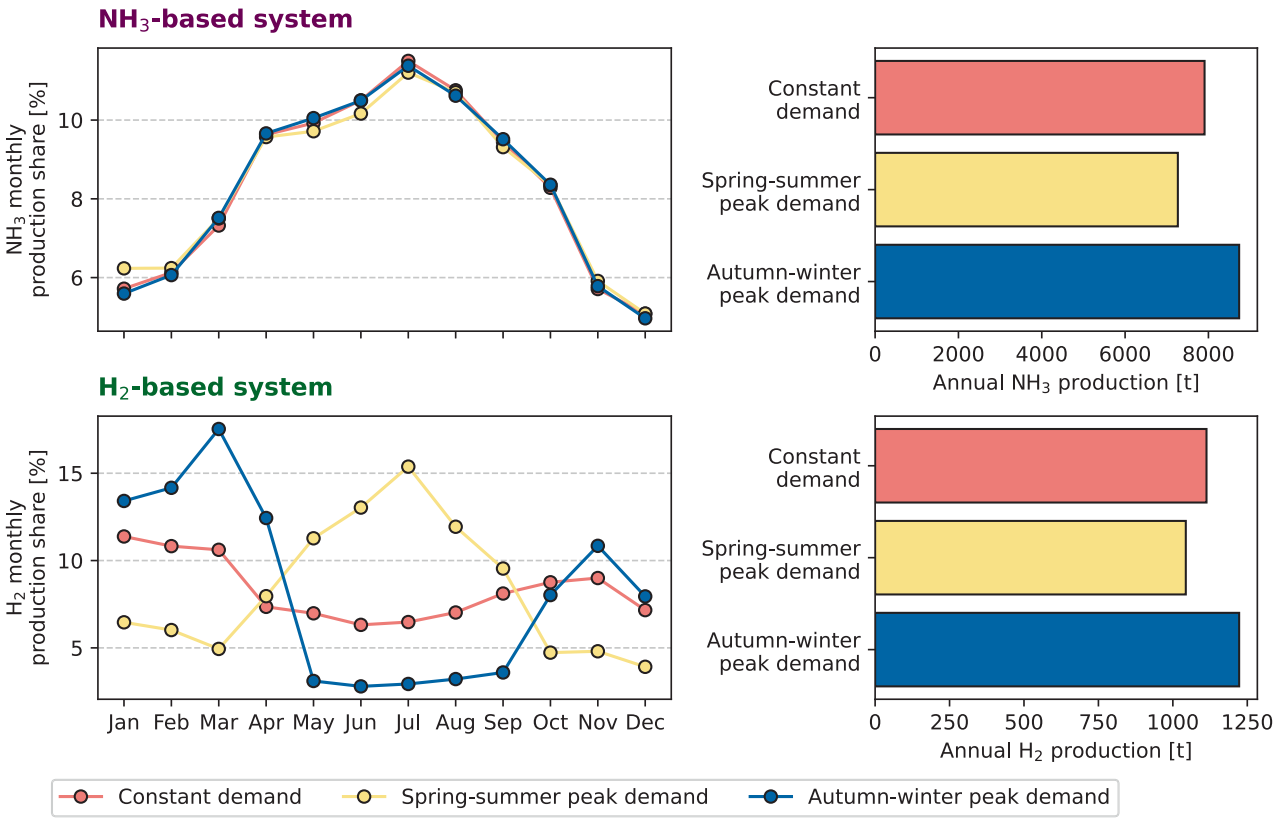

Fig. 20. Monthly production shares (left) and annual total production (right) of NH_3 (top, ammonia-based system) and H_2 (bottom, hydrogen-based system) under different demand scenarios.

Table 4
Sizing results from LCOE minimization for different demand profiles, without a battery and with an 8-hour battery. Base case results (no battery) are shown on the left, new results (with battery) appear in bold to the right of the arrow. If no arrow is shown, results are unchanged. Const. = constant demand case, Summ. = summer-peaked demand case, Wint. = winter-peaked demand case.

Component	Ammonia-based system			Hydrogen-based system		
	Const.	Summ.	Wint.	Const.	Summ.	Wint.
PV [MW]	96 → **75**	85 → **57**	118 → **103**	120 → **105**	58 → **43**	**150**
PEMEL [MW]	30 → **20**	29 → **10**	33 → **19**	40 → **30**	25 → **12**	62 → **54**
H_2 Tank [t]	23 → **16**	16 → **3**	25 → **10**	63 → **49**	32 → **26**	285 → **155**
PSA [n°]	3 x 400 Nm^3_{N2}/h → **2 x 400 Nm^3_{N2}/h**	3 x 400 Nm^3_{N2}/h → **3 x 100 Nm^3_{N2}/h**	4 x 400 Nm^3_{N2}/h → **2 x 300 Nm^3_{N2}/h**	–	–	–
ASR [kg/s]	0.50 → **0.30**	0.46 → **0.12**	0.54 → **0.25**	–	–	–
NH_3 Tank [t]	1660 → **1380**	620 → **720**	3765 → **2765**	–	–	–
CCGT [MW]	4.65 → **4.30**	8.60 → **8.10**	8.72 → **8.30**	**4**	**8**	**8**
LCOE [€/kWh]	0.529→ **0.457**	0.483→ **0.389**	0.666→ **0.601**	0.575→ **0.524**	0.343→ **0.362**	1.209→ **1.021**

with its higher round-trip efficiency, shifts part of the winter balancing from long-term chemical storage to short–term battery storage. In the summer-peaked scenario, however, the battery cannot replace a larger share of long-term storage, since chemical storage already provided significant short-term balancing due to the load profile. In the ammonia-based system, this leads to larger tanks: despite a smaller reactor, more ammonia is accumulated during winter, when the lower electrical load is largely met by the battery. As a result, the system stores more ammonia for summer than in the base case, even with reduced PV generation in winter. The optimization ensures that ammonia is never discarded and the reactor is never oversized, taking advantage of the relatively low cost of tanks. This effect does not occur in the hydrogen-based case, where the optimization consistently minimizes tank size.

Fig. 22 reports the resulting LCOE for the three load profile cases, comparing systems with and without battery integration. The bars indicate the percentage increase or decrease in LCOE of the battery-integrated case relative to the base case, broken down by component contributions. Except for the hydrogen-based system under the summer-peaked demand, battery integration reduces the LCOE, with the magnitude of the reduction depending on both the load profile and the storage technology.

The ammonia-based system benefits more from the introduction of a short-term balancing technology with higher round-trip efficiency. Ammonia is otherwise uneconomical for short-term storage due to system complexity and low round-trip efficiency. This is particularly evident in the summer-peaked scenario, where the LCOE decreases by about 20 %. Here, short-term balancing requirements are high and are largely shifted to the battery, resulting in significant reductions in the contributions from PV, electrolyzer, and ammonia plant to the LCOE. Although the LCOS increases from 0.377 €/kWh to 0.436 €/kWh, the reduction in PV and electrolyzer capacity drives the overall LCOE down. In the constant demand and winter-peaked scenarios, the ΔLCOE remains negative but smaller, as battery integration again raises LCOS (from 0.377 to 0.389 €/kWh and from 0.472 to 0.495 €/kWh, respectively) while the reduction in PV and electrolyzer contributions is less pronounced. Notably, the scenario in which ammonia achieves the largest LCOE reduction is also the only one in which the reliance on long–term storage increases. In the hydrogen-based system, the battery lowers the system sizes mainly through the displacement of storage

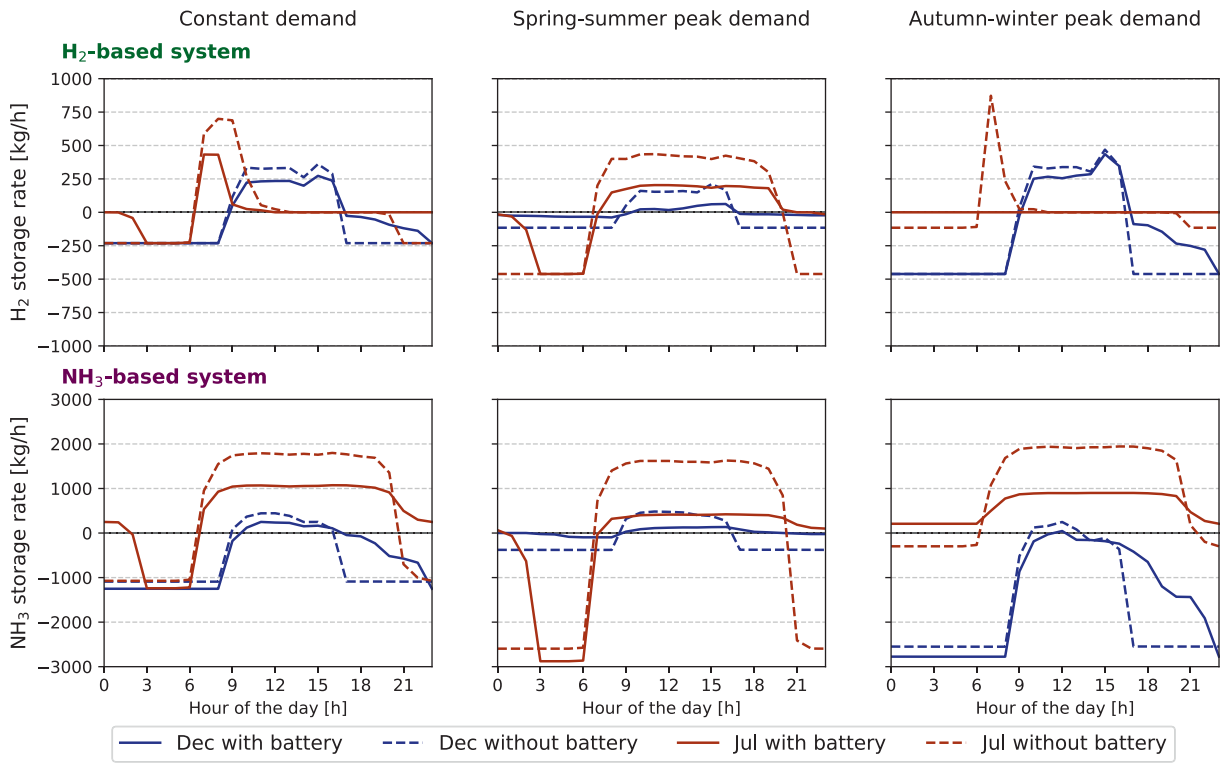

Fig. 21. Average hourly storage rates in hydrogen tank for the H_2-based system (top row) and ammonia tank for the NH_3-based system (bottom row) under the three electricity demand scenarios. A positive value means the tank is charging. Curves represent mean daily values for December (blue) and July (brown), with solid lines indicating configurations with battery storage and dashed lines without.

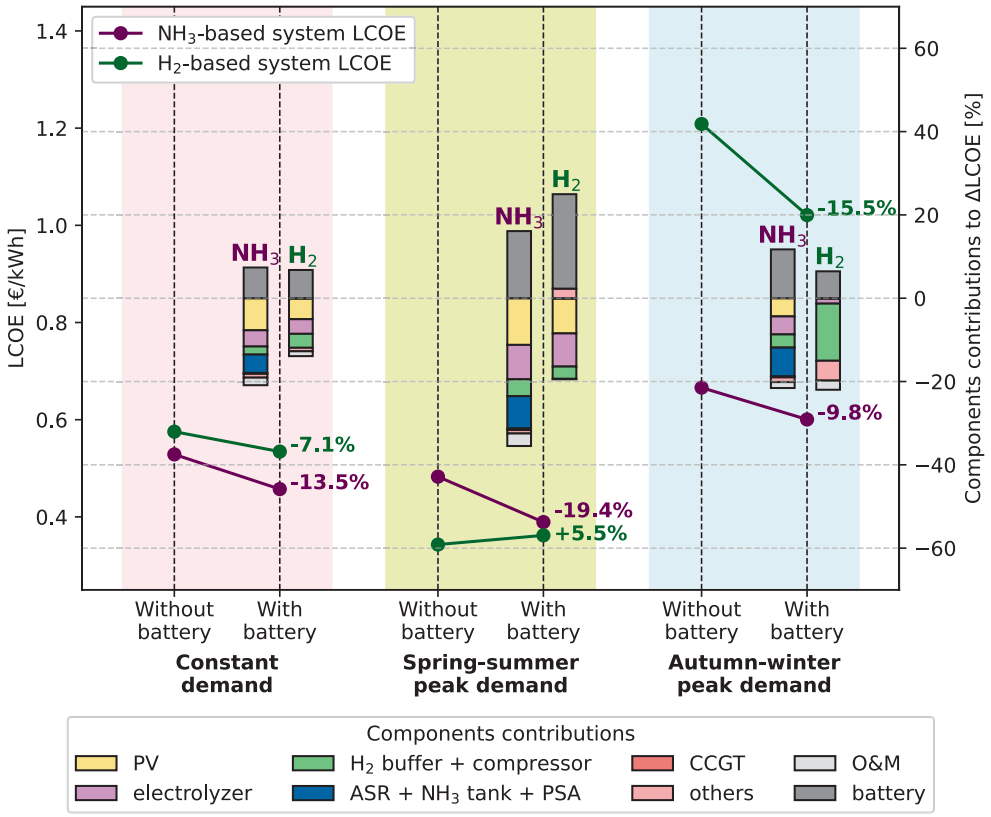

Fig. 22. Markers show LCOE values (left y-axis) under different demand scenarios, comparing cases with and without a battery. Stacked bars (right y-axis) display the individual contributions of each system component to the ΔLCOE, calculated as the difference between LCOE with and without a battery, normalized by the LCOE without a battery.

previously covered by long-term hydrogen, rather than by providing a real advantage from its higher round-trip efficiency in short-term balancing. In fact, the largest LCOE reduction for the hydrogen-based system occurs in the winter-peaked scenario, cutting tank costs (Fig. 22). In this case, the LCOS drops from 1.01 €/kWh to 0.763 €/kWh. In the summer–peaked scenario instead, the LCOE worsens because the cost of battery integration is not sufficiently offset by reductions in other components. Correspondingly, the LCOS rises sharply, from 0.239 €/kWh to 0.338 €/kWh. Under constant demand, the hydrogen-based system achieves a moderate LCOE reduction, with only a marginal change in LCOS (from 0.315 €/kWh to 0.311 €/kWh). This improvement is primarily driven by lower PV and electrolyzer contributions, even though the LCOS increases slightly.

Even with these absolute changes in the LCOE of the battery-integrated case, the relative comparison between the hydrogen-based and ammonia-based systems remains unchanged: ammonia is still more cost-effective in the constant demand and winter-peaked scenarios.

4. Conclusions

This study analyzed the techno-economic viability of green ammonia as an energy storage vector compared to compressed hydrogen, across different electricity demand profiles. Although ammonia conversion introduces additional process complexity and energy losses, its main advantage lies in drastically lower tank cost, making it a compelling solution for seasonal energy storage applications.

A comprehensive Power-to-Ammonia-to-Power model was developed using the simulation framework MESS, allowing full customization of component behavior and system control. The system includes a PV system, a PEMEL, a PSA nitrogen separation unit, H_2 and NH_3 storage tanks, and a Haber–Bosch ammonia synthesis reactor (ASR) modeled with detailed thermodynamics and kinetics, operating in an adiabatic indirectly cooled configuration at typical industrial conditions (150–300 bar, 400–500 °C). Off-design behavior and operational constraints, such as minimum reactor load and ramping limitations, were explicitly modeled, enabling an accurate representation of system flexibility and energy use.

Energy consumption analysis showed that, at nominal conditions, ammonia synthesis requires ~ 0.35 kWh/kg_{NH3}, with the electrolyzer being by far the most energy-intensive component (~55 kWh/kg_{H2}). However, the key economic driver is ammonia tank cost, which is ~ 5 €/kg_{NH3} (0.96 €/kWh), far lower than compressed hydrogen storage (470 €/kg_{H2} at 200 bar, corresponding to ~ 14 €/kWh). This cost difference drives optimal component sizing and leads to different storage strategies depending on the storage medium.

Three electricity demand profiles were studied: constant, summer-peaked, and winter-peaked. In all cases, PV oversizing is used to cover storage needs, as no grid connection is assumed. In the hydrogen–based system, economic optimization favors daily cycling, since large-scale hydrogen storage is prohibitively expensive.

In contrast, ammonia storage enables more seasonal storage due to its much cheaper tank costs. However, a key constraint is the limited flexibility of the ASR, which cannot be shut down and requires a continuous minimum hydrogen feed. This poses a limitation on the ability to shift ammonia production to periods of high renewable availability.

The ASR control strategy developed consists in reducing reactor load when hydrogen buffer levels are low. This allows more efficient use of hydrogen and better alignment of ammonia production with renewable availability. Results show that without such control, ammonia storage is less competitive than hydrogen. However, with control, the ammonia-based system becomes more economical in most cases.

Specifically:

- In the constant-demand case, reactor control (triggered at 90 % buffer level) reduces LCOE for ammonia to 0.529 €/kWh, beating hydrogen at 0.575 €/kWh. Without control, the opposite holds.
- In the winter-peaked case, ammonia shows a strong advantage (0.666 €/kWh) due to the ability to store energy over long durations at low cost, while hydrogen becomes economically unfeasible (1.209 €/kWh), mostly due to expensive tank capacity.
- In the summer-peaked case, with fewer long-term storage requirements, hydrogen is superior (0.343 €/kWh) thanks to higher round–trip efficiency and lower system complexity, while ammonia reaches 0.483 €/kWh, penalized by synthesis energy cost and additional CAPEX costs.

In addition to the base case, a battery-integrated case was considered to provide short-term balancing with higher round-trip efficiency storage. The LCOE decreases in all scenarios except for the hydrogen–based system under the summer–peaked load profile, while the relative comparison between ammonia-based and hydrogen-based systems remains unchanged across all three load profiles.

These results underline that storage economics are not only a matter of conversion efficiency, but are heavily influenced by storage cost, process flexibility, and system control. Ammonia becomes attractive when long-duration storage is required, and its competitiveness is enhanced through smart ASR management that reduces dependency on large hydrogen buffers.

From a broader perspective, ammonia-based systems could serve as an enabling technology for off–grid renewable energy autonomy, remote area electrification, and decarbonization of energy–intensive industries. Future research should consider transportation, multi-vector storage, and advanced ammonia synthesis reactor technologies capable of dynamic operation, allowing ammonia to evolve into a more versatile energy carrier capable of responding dynamically to variable energy supply and demand conditions.

CRediT authorship contribution statement

Valentina Veltroni: Conceptualization, data curation, formal analysis, investigation, methodology, software, visualization, writing – original draft. **Mattia Calabrese:** Writing – review & editing, Software, Methodology, Investigation, Data curation. **Carlo Carcasci:** Writing – review & editing, Supervision, Methodology. **Marco Pagliai:** Writing – review & editing, Validation, Supervision, Methodology.

Funding

This work received funding from the European Union's HORIZON EUROPE Research and Innovation Programme under grant agreement no. 101137625 (ACHIEVE).

Declaration of competing interest

The authors declare that they have no known competing financial interests or personal relationships that could have appeared to influence the work reported in this paper.

Appendix A

This appendix provides the validation of the kinetic model developed for the catalytic beds of the HB reactor by comparing its predictions with both

experimental and modeling data available in the literature. The input parameters used for the validation are consistent with those reported by Jorqueira et al. [54], which refers to the same industrial catalytic beds modeled by Singh and Saraf [66]. The comparison focuses on key variables such as temperature and conversion profiles along the beds, with the objective of verifying the model ability to accurately reproduce the behavior of the real system under typical operating conditions. The inputs considered include the volume and inlet temperature of the three adiabatic beds, as well as the composition, mass flow rate, and pressure of the reactants at first bed inlet as reported in Table A.1 and Table A.2.

Table A1
Parameters of the three beds used for model validation [54,66].

Bed	V [m^3]	T_{in} [K]
1	4.75	658.15
2	7.2	706.15
3	7.8	688.15

Table A2
First bed input parameters used for model validation [54,66].

Parameter	Value
y_{N_2}	0.2219
y_{H_2}	0.6703
y_{NH_3}	0.0276
y_{CH_4}	0.0546
y_{Ar}	0.0256
$\dot{m}$[kg/s]	29.821
p[atm]	226

For the first bed, the nitrogen conversion rate is initially set to zero. For the subsequent beds, all the input conditions are taken from the output of the previous bed, except for the temperature and volume, which are fixed in advance.

The results obtained are in close agreement with those of the actual industrial plant reported by Singh and Saraf [66] as shown in Table A.3 as well as in Fig. A.1 and Fig. A.2.

Table A3
Validation results.

	Bed 1	Bed 2	Bed 3
T_{out} plant [K]	780.15	775.15	728.15
T_{out} model [K]	775.34	780.86	740.02
T_{out} relative error [%]	0.62	0.74	1.63
X_{N_2} plant [%]	15.78	25.55	30.91
X_{N_2} model [%]	15.39	25.13	31.83
X_{N_2} relative error [%]	2.47	1.64	2.98

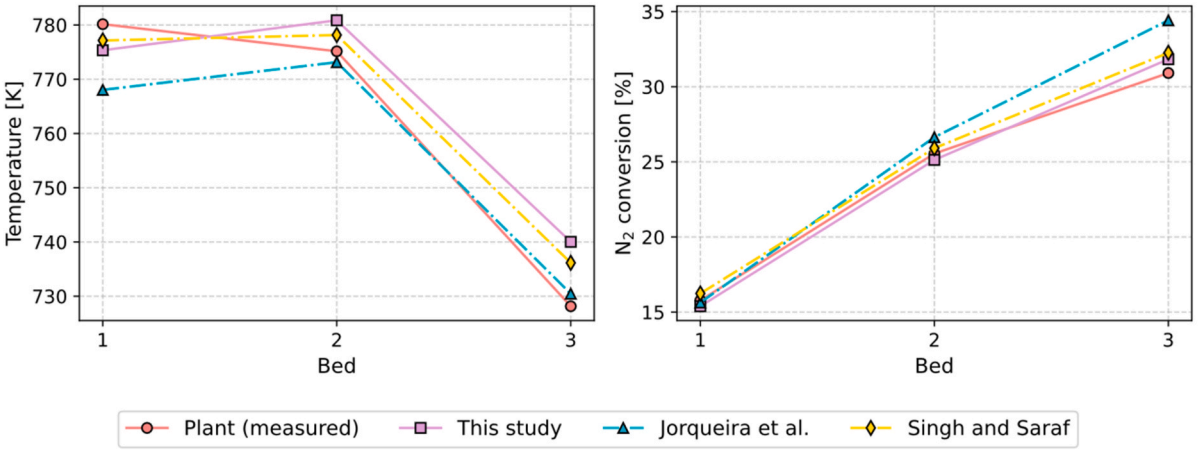

Fig. A1. Comparison of this study results with literature data and real plant measurements. Temperature exiting the beds (left) and nitrogen conversion exiting the beds (right).

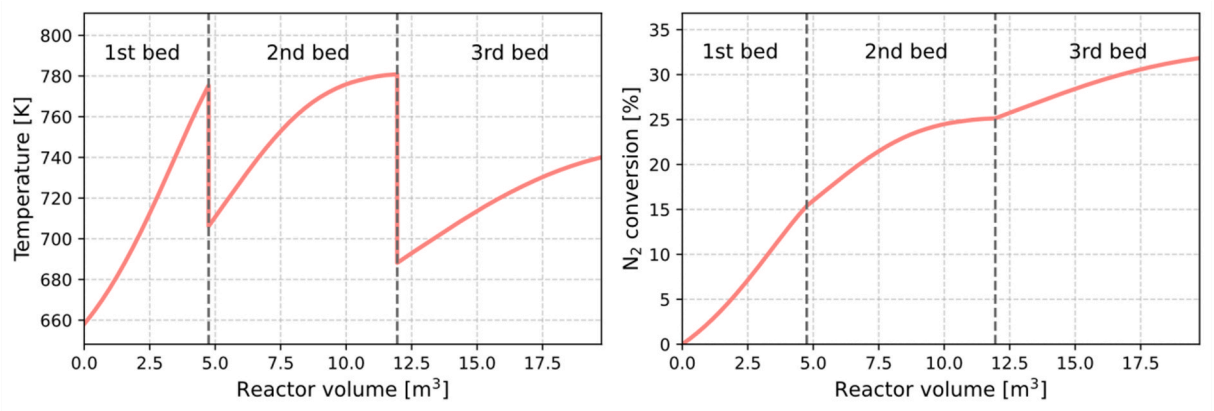

Fig. A2. Temperature (left) and nitrogen conversion (right) profiles along the catalytic beds – results from this study.

Appendix B

This appendix reports the results of a parametric study on the effect of the operating pressure in a HB ammonia synthesis reactor producing 1 kg_{NH3}/s, with operating pressures of the catalytic beds ranging from 150 to 300 bar. The inlet temperatures of the three catalytic beds are maintained at 390 °C, 420 °C, and 410 °C respectively throughout the analysis. The volumes of the three beds are adjusted at each pressure level to maintain a constant degree of approach to equilibrium compared to the reference case at 150 bar (Section 2.8.3.). Specifically, the equilibrium achievement levels are approximately 70 % in the first bed, 97 % in the second bed, and 96 % in the third bed. The degree of equilibrium achievement is defined as the ratio between the nitrogen conversion at the bed outlet and the theoretical conversion at equilibrium, where the net reaction rate becomes zero [78]. The ammonia condensation temperature is optimized for each pressure value to ensure that the molar concentration of ammonia in the recycled gas stream remains at 4 %. As the operating pressure increases, the partial pressure of ammonia in the gas phase also increases, allowing condensation to occur at higher temperatures. Consequently, the refrigeration cycle can operate at elevated temperatures, reducing the required cooling duty. This trend is illustrated in Fig. B.1.

The ammonia synthesis reaction proceeds with a net reduction in the number of moles (from 4 mol of reactants to 2 mol of product). According to Le Chatelier's principle, increasing the operating pressure shifts the equilibrium toward the product side, thereby enhancing the conversion of nitrogen and hydrogen into ammonia. As a consequence, the rate of ammonia formation increases with pressure due to the higher fugacities of the reactants relative to that of the product, as shown in Equation (5).

An increase in r_{NH_3} reduces the residence time required to reach a given percentage of equilibrium, which in turn allows for smaller beds volumes to achieve the same extent of conversion. This trend is evident in Fig. B.2. Additionally, the equilibrium position itself is pressure-dependent: at higher pressures, the same relative proximity to equilibrium corresponds to a higher absolute value of nitrogen conversion (Fig. B.2). As a result, the required recycle ratio decreases as shown in Fig. B.1.

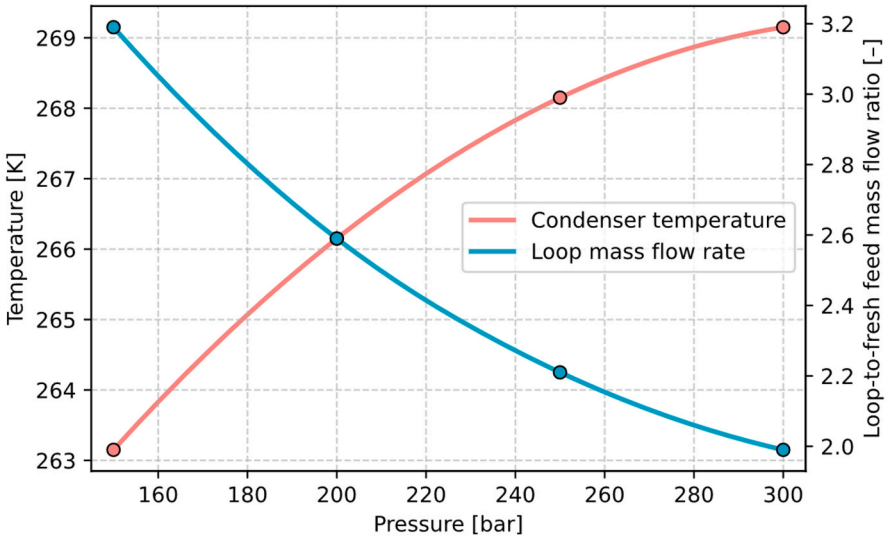

Fig. B1. Condenser temperature (red line) and loop-to-fresh feed mass flowrate ratio (sky-blue line) depending on the operating pressure.

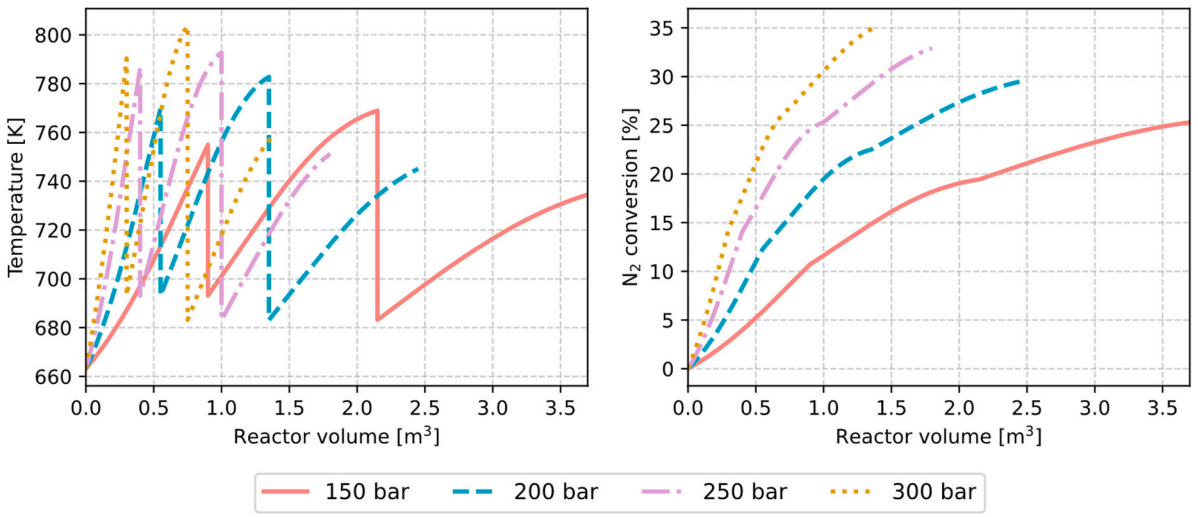

Fig. B2. Temperature (left) and nitrogen conversion profiles (right) depending on the operating pressure for an ammonia synthesis reactor producing 1 kg_{NH3}/s.

The trend of electricity consumption as a function of pressure reveals distinct contributions from various process units (Fig. B.3). As the operating pressure increases, the power demand of the fresh feed compressors rises significantly, primarily due to the higher compression work required to reach elevated pressures. Conversely, the load on the refrigeration system decreases with pressure, which can be attributed to two factors: reduced recirculation flow and higher condensing temperatures, both of which diminish the condenser duty. Similarly, the power required by the loop compressor declines at higher pressures. This reduction is driven by the lower volumetric flow rate being recycled, despite a slight increase in the compression ratio associated with pressure losses, assumed as 6 % of the operating pressure. Overall, the total electricity consumption increases with pressure, as the additional work required by the feed compressors outweighs the energy savings from reduced recirculation and refrigeration demands.

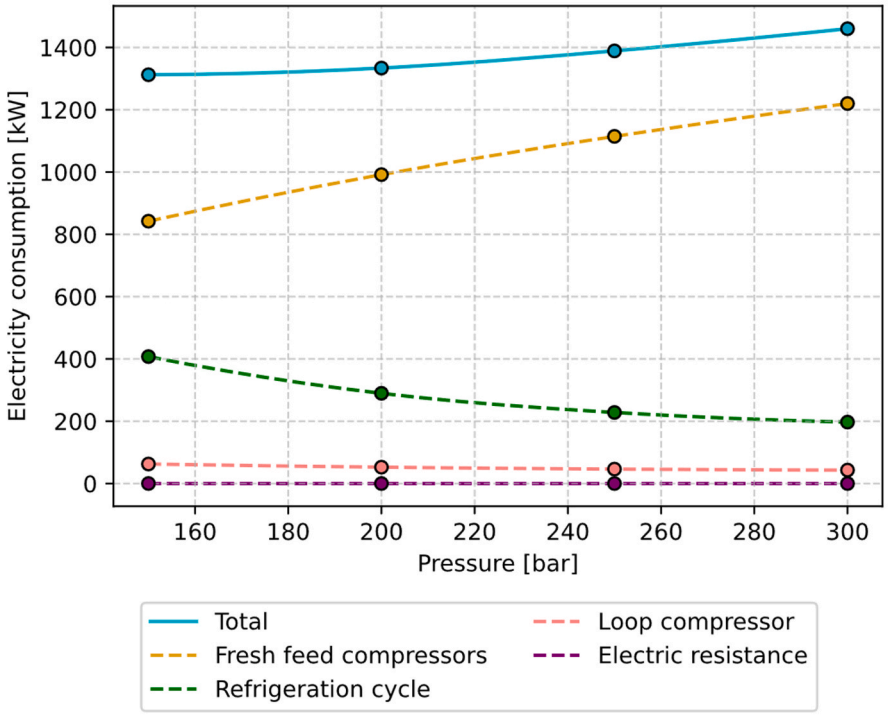

Fig. B3. Total electricity consumption (solid line) and component-wise consumption (dashed lines) as a function of operating pressure for an ammonia synthesis reactor producing 1 kg_{NH3}/s.

As previously discussed, high temperatures promote catalyst deactivation. For this reason, the upper temperature limit is set at 525 °C [54], which represents the maximum allowable temperature within the catalyst bed. Under partial load conditions, the residence time of the reactant gases increases, enhancing reaction conversion and, consequently, leading to higher temperature profiles within the catalytic beds. However, at pressures exceeding 150 bar and under minimum load conditions, the temperature surpasses the maximum allowable threshold, as illustrated in Fig. B.4.

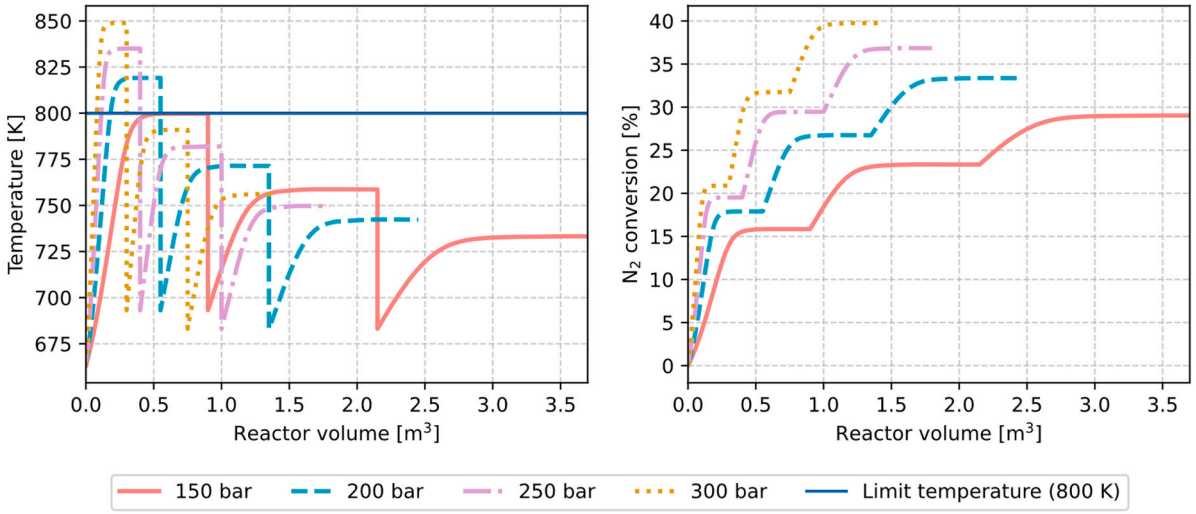

Fig. B4. Temperature (left) and nitrogen conversion profiles (right) depending on the operating pressure at minimum load (30 %) for an ammonia synthesis reactor producing 1 kg_{NH3}/s.

Therefore, adopting an operating pressure of 150 bar enables the system to remain within the maximum allowable temperature limits without the need for additional control mechanisms, while also maximizing energy savings.

Appendix C. Supplementary data

Supplementary data to this article can be found online at https://doi.org/10.1016/j.enconman.2025.120621.

Data availability

Data will be made available on request.

References

[1] Fit for 55 - The EU's plan for a green transition . European Council 2024. https://www.consilium.europa.eu/en/policies/fit-for-55/ (accessed April 20, 2025).
[2] Mekonnin A, Wacławiak K, Humayun M, Zhang S, Ullah H. Hydrogen storage technology, and its challenges: a review. Catalysts 2025;15:260. https://doi.org/10.3390/catal15030260.
[3] Estevez R, López-Tenllado FJ, Aguado-Deblas L, Bautista FM, Romero AA, Luna D. Current Research on Green Ammonia (NH3) as a Potential Vector Energy for Power Storage and Engine Fuels: A Review. Energies (Basel) 2023;16:5451. https://doi.org/10.3390/EN16145451.
[4] Ishaq H, Crawford C. Review and evaluation of sustainable ammonia production, storage and utilization. Energy Convers Manag 2024;300. https://doi.org/10.1016/j.enconman.2023.117869.
[5] Juangsa FB, Irhamna AR, Aziz M. Production of ammonia as potential hydrogen carrier: Review on thermochemical and electrochemical processes. Int J Hydrogen Energy 2021;46:14455–77. https://doi.org/10.1016/J.IJHYDENE.2021.01.214.
[6] Zhou J, Zhang Z, Zhang R, Zhang W, Xu G. Optimal capacity and multi-stable flexible operation strategy of green ammonia systems: Adapting to fluctuations in renewable energy. Energy Convers Manag 2024;314:118720. https://doi.org/10.1016/j.enconman.2024.118720.
[7] Rouwenhorst KHR, Krzywda PM, Benes NE, Mul G, Lefferts L. Ammonia Production Technologies. Techno-Economic Challenges of Green Ammonia as an Energy Vector. Elsevier 2020:41–83. https://doi.org/10.1016/B978-0-12-820560-0.00004-7.
[8] Tawalbeh M, Murtaza SZM, Al-Othman A, Alami AH, Singh K, Olabi AG. Ammonia: A versatile candidate for the use in energy storage systems. Renew Energy 2022;194:955–77. https://doi.org/10.1016/j.renene.2022.06.015.
[9] Negro V, Noussan M, Chiaramonti D. The Potential Role of Ammonia for Hydrogen Storage and Transport: A Critical Review of Challenges and Opportunities. Energies (Basel) 2023;16:6192. https://doi.org/10.3390/EN16176192.
[10] Osman O, Sgouridis S, Sleptchenko A. Scaling the production of renewable ammonia: A techno-economic optimization applied in regions with high insolation. J Clean Prod 2020;271. https://doi.org/10.1016/j.jclepro.2020.121627.
[11] Bouaboula H, Ouikhalfan M, Saadoune I, Chaouki J, Zaabout A, Belmabkhout Y. Addressing sustainable energy intermittence for green ammonia production. Energy Rep 2023;9:4507–17. https://doi.org/10.1016/j.egyr.2023.03.093.
[12] Sahu S, Srivastava N, Arora P, Natu I, Bhosale AC, Singh R, et al. Techno-enviro-economic evaluation of decentralized solar ammonia production plant in India under various energy supply scenarios. Energy Convers Manag 2024;318:118908. https://doi.org/10.1016/J.ENCONMAN.2024.118908.
[13] Sánchez A, Martín M. Optimal renewable production of ammonia from water and air. J Clean Prod 2018;178:325–42. https://doi.org/10.1016/j.jclepro.2017.12.279.
[14] Fúnez Guerra C, Reyes-Bozo L, Vyhmeister E, Jaén Caparrós M, Salazar JL, Clemente-Jul C. Technical-economic analysis for a green ammonia production plant in Chile and its subsequent transport to Japan. Renew Energy 2020;157:404–14. https://doi.org/10.1016/j.renene.2020.05.041.
[15] Kakavand A, Sayadi S, Tsatsaronis G, Behbahaninia A. Techno-economic assessment of green hydrogen and ammonia production from wind and solar energy in Iran. Int J Hydrogen Energy 2023;48:14170–91. https://doi.org/10.1016/j.ijhydene.2022.12.285.
[16] Smith C, Torrente-Murciano L. Cost efficiency versus energy utilization in green ammonia production from intermittent renewable energy. Nature Chemical Engineering 2025 2:4 2025;2:261–72. Doi: 10.1038/s44286-025-00207-9.
[17] Smith C, Torrente-Murciano L. The importance of dynamic operation and renewable energy source on the economic feasibility of green ammonia. Joule 2024;8:157–74. https://doi.org/10.1016/j.joule.2023.12.002.
[18] Tully Z, King J, Johnson K. Hydrogen storage minimization under industrial flexibility constraints: A techno-economic analysis of off-grid green ammonia production. Int J Hydrogen Energy 2025;111:12–21. https://doi.org/10.1016/j.ijhydene.2025.02.109.
[19] Campion N, Nami H, Swisher PR, Vang Hendriksen P, Münster M. Techno-economic assessment of green ammonia production with different wind and solar potentials. Renew Sustain Energy Rev 2023;173. https://doi.org/10.1016/j.rser.2022.113057.
[20] Armijo J, Philibert C. Flexible production of green hydrogen and ammonia from variable solar and wind energy: Case study of Chile and Argentina. Int J Hydrogen Energy 2020;45:1541–58. https://doi.org/10.1016/j.ijhydene.2019.11.028.
[21] Wang C, Walsh SDC, Longden T, Palmer G, Lutalo I, Dargaville R. Optimising renewable generation configurations of off-grid green ammonia production systems considering Haber-Bosch flexibility. Energy Convers Manag 2023;280. https://doi.org/10.1016/j.enconman.2023.116790.
[22] Wu Y, Zhao T, Tang S, Wang Y, Ma M. Research on design and multi-frequency scheduling optimization method for flexible green ammonia system. Energy Convers Manag 2024;300. https://doi.org/10.1016/j.enconman.2023.117976.
[23] Allman A, Daoutidis P. Optimal scheduling for wind-powered ammonia generation: Effects of key design parameters. Chem Eng Res Des 2018;131:5–15. https://doi.org/10.1016/j.cherd.2017.10.010.
[24] Nayak-Luke R, Bañares-Alcántara R, Wilkinson I. "green" Ammonia: Impact of Renewable Energy Intermittency on Plant Sizing and Levelized Cost of Ammonia. Ind Eng Chem Res 2018;57:14607–16. https://doi.org/10.1021/acs.iecr.8b02447.
[25] Siddiqui O, Dincer I. A new solar energy system for ammonia production and utilization in fuel cells. Energy Convers Manag 2020;208:112590. https://doi.org/10.1016/J.ENCONMAN.2020.112590.

[26] Müller M, Pfeifer M, Holtz D, Müller K. Comparison of green ammonia and green hydrogen pathways in terms of energy efficiency. Fuel 2024;357:129843. https://doi.org/10.1016/J.FUEL.2023.129843.
[27] Tsiklios C, Schneider S, Hermesmann M, Müller TE. Efficiency and optimal load capacity of E-Fuel-Based energy storage systems. Adv Appl Energy 2023;10:100140. https://doi.org/10.1016/J.ADAPEN.2023.100140.
[28] Wen D, Aziz M. Techno-economic analyses of power-to-ammonia-to-power and biomass-to-ammonia-to-power pathways for carbon neutrality scenario. Appl Energy 2022;319:119272. https://doi.org/10.1016/J.APENERGY.2022.119272.
[29] Ikäheimo J, Kiviluoma J, Weiss R, Holttinen H. Power-to-ammonia in future North European 100 % renewable power and heat system. Int J Hydrogen Energy 2018;43:17295–308. https://doi.org/10.1016/j.ijhydene.2018.06.121.
[30] Wen D, Liu S, Ning Z, Aziz M. Techno-economic evaluation of hydrogen and ammonia as energy carriers in a multi-generation system. Energy Convers Manag 2023;277. https://doi.org/10.1016/j.enconman.2023.116670.
[31] Palys MJ, Daoutidis P. Using hydrogen and ammonia for renewable energy storage: A geographically comprehensive techno-economic study. Comput Chem Eng 2020;136. https://doi.org/10.1016/j.compchemeng.2020.106785.
[32] Palys MJ, Kuznetsov A, Tallaksen J, Reese M, Daoutidis P. A novel system for ammonia-based sustainable energy and agriculture: Concept and design optimization. Chem Eng Process - Process Intesif 2019;140:11–21. https://doi.org/10.1016/j.cep.2019.04.005.
[33] Rouwenhorst KHR, Van der Ham AGJ, Mul G, Kersten SRA. Islanded ammonia power systems: Technology review & conceptual process design. Renew Sustain Energy Rev 2019;114. https://doi.org/10.1016/j.rser.2019.109339.
[34] Cesaro Z, Ives M, Nayak-Luke R, Mason M, Bañares-Alcántara R. Ammonia to power: Forecasting the levelized cost of electricity from green ammonia in large-scale power plants. Appl Energy 2021;282. https://doi.org/10.1016/j.apenergy.2020.116009.
[35] Lan P, Chen S, Li Q, Li K, Wang F, Zhao Y, et al. Comparison of different hydrogen-ammonia energy conversion pathways for renewable energy supply. Renew Energy 2024;227:120602. https://doi.org/10.1016/J.RENENE.2024.120602.
[36] Controllability GR. Analysis of Ammonia Synthesis Loops. Norwegian University of Science and Technology; 2018.
[37] Giulia F. Dynamics and Control of a Load Flexible Green Ammonia Plant. Politecnico Di Milano 2024. https://www.politesi.polimi.it/handle/10589/222700 (accessed December 1, 2024).
[38] Patel R, Soleimani Mehr A, Valverde JI, Scheffknecht G, Maier J, Zohourian R. Studying the effect of dynamic operation conditions on green ammonia production synthesis loop. J Process Control 2025;150:103436. https://doi.org/10.1016/J.JPROCONT.2025.103436.
[39] Fahr S, Schiedeck M, Schwarzhuber J, Rehfeldt S, Peschel A, Klein H. Design and thermodynamic analysis of a large-scale ammonia reactor for increased load flexibility. Chem Eng J 2023;471. https://doi.org/10.1016/j.cej.2023.144612.
[40] Fahr S, Schiedeck M, Reinke M, Bohn JP, Rehfeldt S, Peschel A, et al. Simultaneous design and part-load optimization of an industrial ammonia synthesis reactor. Chem Eng J 2024;480. https://doi.org/10.1016/j.cej.2023.148302.
[41] Cheema II, Krewer U. Optimisation of the autothermal NH3 production process for power-to-ammonia. Processes 2020;8. https://doi.org/10.3390/pr8010038.
[42] Cheema II, Krewer U. Operating envelope of Haber-Bosch process design for power-to-ammonia. RSC Adv 2018;8:34926–36. https://doi.org/10.1039/c8ra06821f.
[43] Pasqui M, Mati A, Ademollo A, Calabrese M, Lubello P, Carcasci C. MESS 2024. https://github.com/pielube/MESSpy/tree/main?tab=readme-ov-file (accessed April 20, 2025).
[44] Bottecchia L, Lubello P, Zambelli P, Carcasci C, Kranzl L. The potential of simulating energy systems: The multi energy systems simulator model. Energies (Basel) 2021;14. https://doi.org/10.3390/en14185724.
[45] Lubello P, Pasqui M, Mati A, Carcasci C. Assessment of hydrogen-based long term electrical energy storage in residential energy systems. Smart Energy 2022;8. https://doi.org/10.1016/j.segy.2022.100088.
[46] Ademollo A, Mati A, Pagliai M, Carcasci C. Exploring the role of hydrogen in decarbonizing energy-intensive industries: A techno-economic analysis of a solid oxide fuel cell cogeneration system. J Clean Prod 2024;469. https://doi.org/10.1016/j.jclepro.2024.143254.
[47] Ademollo A, Calabrese M, Carcasci C. An up-to-date perspective of levelized cost of hydrogen for PV-based grid-connected power-to-hydrogen plants across all Italy. Appl Energy 2025;379:124958. https://doi.org/10.1016/J.APENERGY.2024.124958.
[48] Photovoltaic Geographical Information System (PVGIS). European Commission 2024. https://re.jrc.ec.europa.eu/pvg_tools/en/ (accessed November 13, 2024).
[49] Huld T, Müller R, Gambardella A. A new solar radiation database for estimating PV performance in Europe and Africa. Sol Energy 2012;86:1803–15. https://doi.org/10.1016/j.solener.2012.03.006.
[50] Gracia L, Casero P, Bourasseau C, Chabert A. Use of Hydrogen in Off-Grid Locations, a Techno-Economic Assessment. Energies (Basel) 2018;11:3141. https://doi.org/10.3390/EN11113141.
[51] Khan M, Young C, Mackinnon C, Layzell D. The techno-economics of hydrogen compression. accessed January 9, 2025 Transition Accelerator Technical Briefs 2021;1(1):1–36. http://transitionaccelerator.ca/wp-content/uploads/2023/04/TA-Technical-Brief-1.1_TEEA-Hydrogen-Compression_PUBLISHED.pdf.
[52] PPNG 100-800 HE PSA Nitrogen Generators. Pneumatech 2024. https://www.pneumatech.com/en-international/nitrogen-generators/psa-nitrogen-generators/ppng-psa-nitrogen-generators-100-800-he (accessed March 3, 2025).
[53] Rueda S, Miltrup M, Adekanbi A. Ammonia, nitrogen and green hydrogen production & purification. International PtX Hub 2024. https://www.angphotorion.com/wp-content/uploads/2025/04/international-ptx-hub_202401_ammonia-nitrogen-and-green-hydrogen-production-and-purification.pdf (accessed February 16, 2025).
[54] Jorqueira DSS, Neto AMB, Rodrigues MTM. Modeling and Numerical Simulation of Ammonia Synthesis Reactors Using Compositional Approach. Advances in Chemical Engineering and Science 2018;08:124–43. https://doi.org/10.4236/aces.2018.83009.
[55] The Danish Energy Agency. Technology Data for Renewable Fuels 2017. https://ens.dk/en/analyses-and-statistics/technology-data-renewable-fuels (accessed March 28, 2025).
[56] Miltrup P, Rueda S, Rojas A R. Ammonia transport & storage. International PtX Hub 2024. https://www.scribd.com/document/767452703/AMMONIA-TRANSPORT-STORAGE (accessed January 2, 2025).
[57] Shepherd J, Haider Ali Khan M, Amal R, Daiyan R, MacGill I. Open-source project feasibility tools for supporting development of the green ammonia value chain. Energy Convers Manag 2022;274. https://doi.org/10.1016/j.enconman.2022.116413.
[58] Marocco P, Ferrero D, Lanzini A, Santarelli M. Optimal design of stand-alone solutions based on RES + hydrogen storage feeding off-grid communities. Energy Convers Manag 2021;238:114147. https://doi.org/10.1016/J.ENCONMAN.2021.114147.
[59] IRENA and AEA. Innovation outlook : renewable ammonia. International Renewable Energy Agency 2022. https://www.irena.org/publications/2022/May/Innovation-Outlook-Renewable-Ammonia.
[60] Palys MJ, Daoutidis P. Power-to-X: A review and perspective. Comput Chem Eng 2022;165:107948. https://doi.org/10.1016/J.COMPCHEMENG.2022.107948.
[61] Ribeiro C, Santos DMF. Transitioning Ammonia Production: Green Hydrogen-Based Haber–Bosch and Emerging Nitrogen Reduction Technologies. Clean Technol 2025;7:49. https://doi.org/10.3390/CLEANTECHNOL7020049/S1.
[62] Ponikvar Ž, Likozar B, Gyergyek S. Electrification of Catalytic Ammonia Production and Decomposition Reactions: From Resistance, Induction, and Dielectric Reactor Heating to Electrolysis. ACS Appl Energy Mater 2022;5:5457–72. https://doi.org/10.1021/ACSAEM.1C03045/ASSET/IMAGES/LARGE/AE1C03045_0007.JPEG.
[63] Morud JC, Skogestad S. Analysis of instability in an industrial ammonia reactor. AIChE J 1998;44:888–95. https://doi.org/10.1002/AIC.690440414.
[64] Liu X, Elgowainy A, Wang M. Life cycle energy use and greenhouse gas emissions of ammonia production from renewable resources and industrial by-products. Green Chem 2020;22:5751–61. https://doi.org/10.1039/d0gc02301a.
[65] Smith C, Hill AK, Torrente-Murciano L. Current and future role of Haber-Bosch ammonia in a carbon-free energy landscape. Energy Environ Sci 2020;13:331–44. https://doi.org/10.1039/c9ee02873k.
[66] Singh P, CP, Saraf DN. Simulation of Ammonia Synthesis Reactors. Ind Eng Chem Process Des Dev 1979;18:364–70. https://doi.org/10.1021/i260071a002.
[67] Dyson DC, Simon JM. Kinetic expression with diffusion correction for ammonia synthesis on industrial catalyst. Ind Eng Chem, Fundam; (United States) 1968;7(4):605–10. https://doi.org/10.1021/i160028a013.
[68] Rosbo JW, Ritschel TKS, Hørsholt S, Huusom JK, Jørgensen JB. Flexible operation, optimisation and stabilising control of a quench cooled ammonia reactor for power-to-ammonia. Comput Chem Eng 2023;176. https://doi.org/10.1016/j.compchemeng.2023.108316.
[69] Kim J, Huh C, Management YS-EC and, 2022 undefined. End-to-end value chain analysis of isolated renewable energy using hydrogen and ammonia energy carrier. Energy Convers Manag 2022;254:115247. Doi: 10.1016/j.enconman.2022.115247.
[70] Valera-Medina A, Xiao H, Owen-Jones M, David WIF, Bowen PJ. Ammonia for power. Prog Energy Combust Sci 2018;69:63–102. https://doi.org/10.1016/J.PECS.2018.07.001.
[71] Joseph Sekhar S, Samuel MS, Glivin G, Le TG, Mathimani T. Production and utilization of green ammonia for decarbonizing the energy sector with a discrete focus on Sustainable Development Goals and environmental impact and technical hurdles. Fuel 2024;360:130626. https://doi.org/10.1016/J.FUEL.2023.130626.
[72] Pashchenko D. Ammonia fired gas turbines: Recent advances and future perspectives. Energy 2024;290:130275. https://doi.org/10.1016/J.ENERGY.2024.130275.
[73] IEA. Global Hydrogen Review 2024 2024. https://www.iea.org/reports/global-hydrogen-review-2024 (accessed December 10, 2024).
[74] Paulson JA, Tsay C. Bayesian optimization as a flexible and efficient design framework for sustainable process systems. Curr Opin Green Sustain Chem 2025;51:100983. https://doi.org/10.1016/j.cogsc.2024.100983.
[75] Griffith A. Utilizing Bayesian Optimization in Technoeconomic Analyses for Integrated Energy Systems. Utah State University 2024. https://digitalcommons.usu.edu/etd2023/221/ (accessed June 10, 2025).
[76] Akiba T, Sano S, Yanase T, Ohta T, Koyama M. Optuna: A Next-generation Hyperparameter Optimization Framework. Proceedings of the ACM SIGKDD International Conference on Knowledge Discovery and Data Mining 2019:2623–31. https://doi.org/10.1145/3292500.3330701.
[77] Jülch V. Comparison of electricity storage options using levelized cost of storage (LCOS) method. Appl Energy 2016;183:1594–606. https://doi.org/10.1016/J.APENERGY.2016.08.165.
[78] Nicol W, Hildebrandt D, Glasser D. Crossing reaction equilibrium in an adiabatic reactor system. Dev Chem Eng Miner Process 1998;6:41–54. https://doi.org/10.1002/APJ.5500060104.